

Title: A Synthetic Data-Driven Radiology Foundation Model for Pan-tumor Clinical Diagnosis

Wenhui Lei^{1,2*}, Hanyu Chen^{3*}, Zitian Zhang^{4*}, Luyang Luo^{5*}, Qiong Xiao³, Yannian Gu¹, Peng Gao³, Yankai Jiang², Ci Wang⁴, Guangtao Wu³, Tongjia Xu³, Yingjie Zhang³, Pranav Rajpurkar⁵, Xiaofan Zhang^{1,2#}, Shaoting Zhang^{1#}, Zhenning Wang^{3#}

¹Shanghai Jiao Tong University, Shanghai, P.R. China

²Shanghai AI Lab, Shanghai, P.R. China

³Department of Surgical Oncology and General Surgery, Key Laboratory of Precision Diagnosis and Treatment of Gastrointestinal Tumors, Ministry of Education, The First Hospital of China Medical University, Liaoning, P.R. China

⁴Department of Radiology, The First Hospital of China Medical University, Liaoning, P.R. China

⁵Harvard Medical School, Boston, MA, USA

*Contributed equally as first authors

#Correspondence to Xiaofan Zhang, Shaoting Zhang or Zhenning Wang

Keywords: Pan-Tumor Foundation Model, Synthetic Data, Computed Tomography, Oncology AI

Abstract

AI-assisted imaging made substantial advances in tumor diagnosis and management. However, a major barrier to developing robust oncology foundation models is the scarcity of large-scale, high-quality annotated datasets, which are limited by privacy restrictions and the high cost of manual labeling. To address this gap, we present PASTA, a pan-tumor radiology foundation model built on PASTA-Gen, a synthetic data framework that generated 30,000 3D CT scans with pixel-level lesion masks and structured reports of tumors across ten organ systems. Leveraging this resource, PASTA achieves state-of-the-art performance on 45 of 46 oncology tasks, including non-contrast CT tumor screening, lesion segmentation, structured reporting, tumor staging, survival prediction, and MRI-modality transfer. To assess clinical applicability, we developed PASTA-AID, a clinical decision support system, and ran a retrospective simulated clinical trial across two scenarios. For pan-tumor screening on plain CT with fixed reading time, PASTA-AID increased radiologists' throughput by 11.1–25.1% and improved sensitivity by 17.0–31.4% and precision by 10.5–24.9%; additionally, in a diagnosis-aid workflow, it reduced segmentation time by up to 78.2% and reporting time by up to 36.5%. Beyond gains in accuracy and efficiency, PASTA-AID narrowed the expertise gap, enabling less-experienced radiologists to approach expert-level performance. Together, this work establishes an end-to-end, synthetic data-driven pipeline spanning data generation, model development, and clinical validation, thereby demonstrating substantial potential for pan-tumor research and clinical translation.

Main Text

Malignant tumors remain one of the leading causes of death worldwide, placing substantial medical and economic burdens on healthcare systems¹. Radiologic examination, exemplified by computed tomography (CT), plays a key role in oncology by supporting tumor detection, staging, treatment planning, response assessment, and follow-up. In recent years, artificial intelligence (AI) has been increasingly integrated into radiology imaging interpretation, with the aim of improving diagnostic accuracy, efficiency and reproducibility. Task-specific AI models have demonstrated strong performance in organ- and tumor-focused applications, including detection, segmentation and prognostic prediction²⁻⁷. Nevertheless, these models remain constrained by limited disease coverage, heavy dependence on annotated datasets and insufficient generalizability across tumor types and clinical settings.

Foundation models (FMs), pre-trained on large, heterogeneous datasets, have emerged as a powerful paradigm for medical imaging, offering improved label efficiency and robustness across diverse downstream tasks⁸⁻¹⁶. Nevertheless, developing a pan-tumor radiology FM remains challenging, with several obstacles contributing to this gap. On cross-sectional imaging such as CT, tumors often occupy only a small fraction of the volume, and most existing radiology FMs are trained with self-supervised objectives on unlabeled scans¹⁷⁻²⁰. Such objectives tend to emphasize global anatomical structure rather than subtle lesion-specific signals, which limits utility for oncologic imaging. Recent efforts toward supervised foundation models, exemplified by SuPreM²², demonstrate the feasibility of incorporating labeled anatomical or lesion information during pre-training and suggest improved attention to target-region features relative to purely self-supervised counterparts. However, the scarcity of high-quality supervised resources, particularly lesion-level labels and organ-specific annotations across cancer types, restricts the scale of pre-training and narrows tumor coverage, which in turn constrains generalizability. Finally, the development of large, multi-tumor datasets is impeded by the intrinsic rarity of many cancers, the cost of expert annotation, and privacy constraints.

To address these limitations, we developed Pan-tumor Analysis with Synthetic Training Augmentation

(PASTA), a 3D radiology foundation model trained on synthetic lesion data. At the core of this approach is PASTA-Gen, a generative framework that synthesizes realistic malignant and benign lesions across ten organs and fifteen lesion types. Leveraging PASTA-Gen, we constructed PASTA-Gen-30K, a dataset comprising 30,000 synthetic 3D CT scans paired with precise lesion masks and structured textual descriptions. PASTA was pre-trained in two stages—lesion segmentation followed by vision–language alignment—to acquire tumor-centric representations that generalize across diverse tumor types. This design prioritizes fine-grained lesion features while preserving anatomical context, and it yields outputs that map directly to clinical tasks such as screening on non-contrast CT, lesion delineation for treatment planning and structured report generation. To test whether these representations translate into measurable benefits in practice, we further deployed PASTA within a workflow-aligned clinical decision support system.

To evaluate the baseline performance of the PASTA foundation model, we conducted systematic comparisons with leading medical image analysis frameworks, including nnUNet²³, Universal²⁴, and well-established 3D radiology foundation models such as ModelsGenesis²⁰, SuPreM²², and FMCIB²¹. PASTA was further evaluated across 46 downstream tasks, achieving the best performance in 45 of them and significantly outperforming the second-best model in 35, while demonstrating superior few-shot learning efficiency and strong generalization to non-contrast tumor screening, lesion segmentation, structured reporting, tumor staging, survival prediction, and MRI-modality transfer.

Beyond algorithmic benchmarks, real-world deployment demands validation in clinically relevant settings. Foundation models that excel in controlled experiments may still face workflow, efficiency, and accuracy challenges in practice, particularly under time-limited conditions or when assisting radiologists with varying levels of experience. To bridge this gap, we developed PASTA-AID, a clinical decision support system powered by PASTA, and conducted a retrospective simulated clinical trial across two scenarios. In the screening-aid setting, PASTA-AID was evaluated for time-limited non-contrast CT tumor screening. Under a 30-minute high-workload

condition, PASTA-AID improved reading efficiency, recall, and precision. In the diagnosis-aid setting, PASTA-AID was tested on contrast-enhanced CT for tumor segmentation and structured reporting. It significantly reduced segmentation time, with greater time savings for junior than senior radiologists, and markedly improved reporting efficiency across tumor types for radiologists of different experience levels. Importantly, PASTA-AID enhanced the concordance of junior radiologists with senior experts in lesion annotation. These results demonstrate that a synthetic data-driven foundation model-based support system can function not only as a diagnostic reference but also as an efficiency enhancer, alleviating workload and fatigue for radiologists under high-pressure conditions. This collaborative mode is particularly relevant for resource-constrained primary healthcare institutions, underscoring its practical value and translational potential.

Together, these findings establish PASTA as both a methodological advance and a clinically relevant radiology foundation model for oncologic imaging. By publicly releasing PASTA and PASTA-Gen-30K, we provide community resources and evidence that synthetic data-driven pre-training can mitigate annotation scarcity, thereby enabling pan-tumor radiology analysis and accelerating clinical translation.

Results

1. Dataset Generation, Model, and Clinical Decision Support System Development

To link lesion-aware representation learning with measurable clinical benefit, we designed a clinically informed framework that begins with controllable synthesis of realistic CT lesions (PASTA-Gen), scales into a public corpus of image–mask–text pairs (PASTA-Gen-30K), and culminates in a tumor-centric foundation model (PASTA) embedded within a workflow-integrated decision-support system (PASTA-AID) (Fig. 1). PASTA-Gen translates radiology-derived attributes into anatomically grounded simulations within healthy organs, producing paired lesion and organ masks with structured descriptors. These data support supervised two-stage pretraining that emphasizes subtle lesion signal while preserving surrounding context. The resulting capabilities are surfaced

to clinicians through PASTA-AID, which aligns with routine practice to provide assistance for non-contrast CT screening, automated lesion segmentation and structured report drafting. This synthetic-to-clinic design enables a unified assessment of clinical utility across both screening and diagnostic settings.

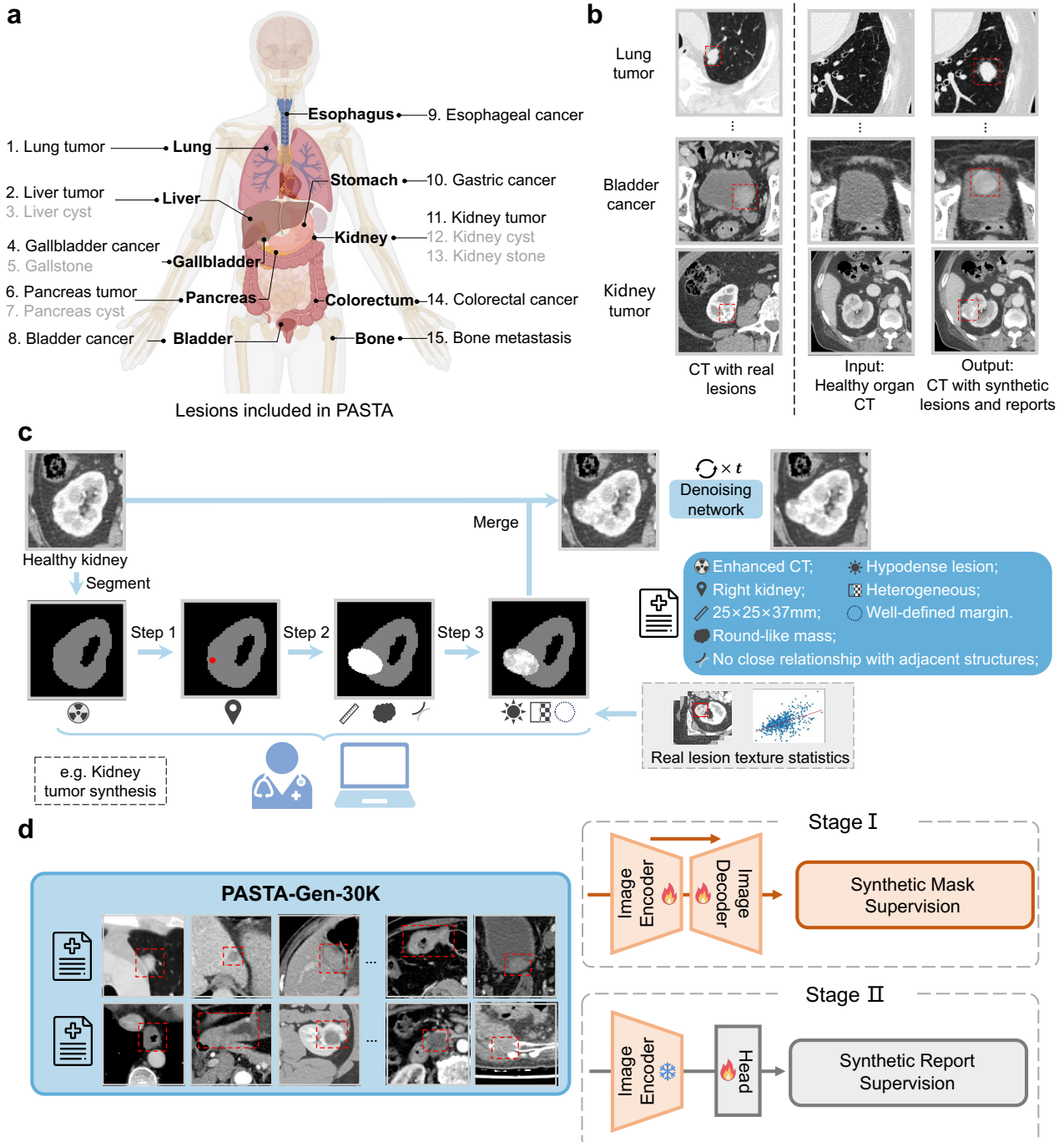


Fig. 1 | Workflow of PASTA Model Development and Training Pipeline. a, Overview of organs and lesion types involved in PASTA training. **b**, Examples of lesions generated by PASTA-Gen from healthy organs. **c**, Lesion generation pipeline of PASTA-Gen. **d**, Two-stage training of PASTA using the PASTA-Gen-30K dataset.

1.1 Construction of PASTA-Gen and PASTA-Gen-30K

To ensure that the synthesized lesions closely match clinical realities, we collected a large set of in-house CT scans paired with radiology reports. Two senior radiologists systematically analyzed the lesion descriptions and identified eight key attributes (e.g., shape, density, density variation) that define solid space-occupying lesions across multiple organs. Building on these findings, we systematically categorized the otherwise varied textual attributes into several structured subcategories, enabling a unified, cross-organ description (Methods and Extended Data Table 1). These structured attributes served as the basis for a universal framework that guided lesion simulation in PASTA-Gen.

During synthesis, we used organ segmentation masks for precise lesion localization. We then applied specific graphical operations to capture the full spectrum of lesion attributes and used a denoising network to enhance image realism (Fig. 1c and Extended Data Fig. 1). Since PASTA-Gen simulates lesions only in corresponding healthy organs, we first gathered 10,767 in-house CT scans along with their radiology reports. From these, we selected subsets containing specific healthy organs for the synthesis task (Extended Data Tables 2 and 3, and Methods).

Based on the PASTA-Gen generative model, we created the PASTA-Gen-30K dataset comprising 30,000 image-mask-text pairs. These include 10 malignancies and 5 benign lesion types, each with 2,000 cases. The dataset provides both lesion and organ masks for each sample and is publicly available. Since it does not contain any real patient data, there are no privacy concerns. Representative samples are shown in Extended Data Fig. 2.

1.2 Construction of PASTA

Using the PASTA-Gen-30K dataset, we trained the PASTA foundation model via a two-stage process focused on both semantic segmentation and text-image alignment. PASTA learns to segment the synthetic lesions from target organs in the first stage and classify their attributes in the second stage. In contrast to previous imaging foundation

models, PASTA leverages a large volume of high-quality synthetic data, overcoming the limitations imposed by data scarcity. Moreover, because tumor lesions constitute only a small fraction of the total CT volume and given the availability of pixel-level lesion masks, PASTA learns the nuanced relationships and subtle differences among lesions, their surrounding tissues, and various tumor types during pre-training. On top of this, PASTA undergoes further training to align lesion-related visual and textual information, facilitating a wide array of downstream tasks (Fig. 1d).

1.3 Construction of PASTA-AID

To evaluate the real-world utility of PASTA, we developed PASTA-AID, a clinical decision support system powered by the foundation model. PASTA-AID is designed to collaborate closely with radiologists and support the entire clinical workflow of tumor management, from screening to diagnostic reporting. Specifically, in the screening setting, it enables rapid lesion detection on non-contrast CT under time-limited conditions, while in the diagnostic setting, it automatically generates lesion masks and structured radiology reports from contrast-enhanced CT scans. Rather than serving as a standalone algorithm, PASTA-AID integrates PASTA's capabilities into a unified platform aligned with radiologists' workflow, with the aims of improving diagnostic efficiency and accuracy, compensating for performance gaps due to limited radiologist experience, and facilitating scalable clinical deployment.

2. Model Performance, Downstream Task and Clinical Evaluation

To characterize both performance and clinical applicability, we undertook a staged evaluation of PASTA, spanning algorithmic benchmarks and workflow-integrated reader studies. The model was first tested across multiple downstream oncological tasks to assess its generalizability. It was then implemented within the PASTA-AID decision-support system and assessed retrospectively in two representative use cases—screening aid on non-contrast CT and diagnosis aid on contrast-enhanced CT—covering detection sensitivity, reading efficiency, lesion segmentation, and structured reporting across radiologists with varying levels of experience.

2.1 Non-contrast CT Tumor Identification

Tumor assessment typically relies on contrast-enhanced CT scans, while routine screenings in hospitals and health check facilities are more often performed with non-contrast CT. However, identifying tumor lesions on non-contrast CT is particularly challenging for both radiologists and current AI algorithms. We evaluated PASTA's performance in distinguishing malignant cases from healthy controls across three cancer types: liver, pancreatic, and kidney cancers (Fig. 2a, b, and Supplementary Table 1).

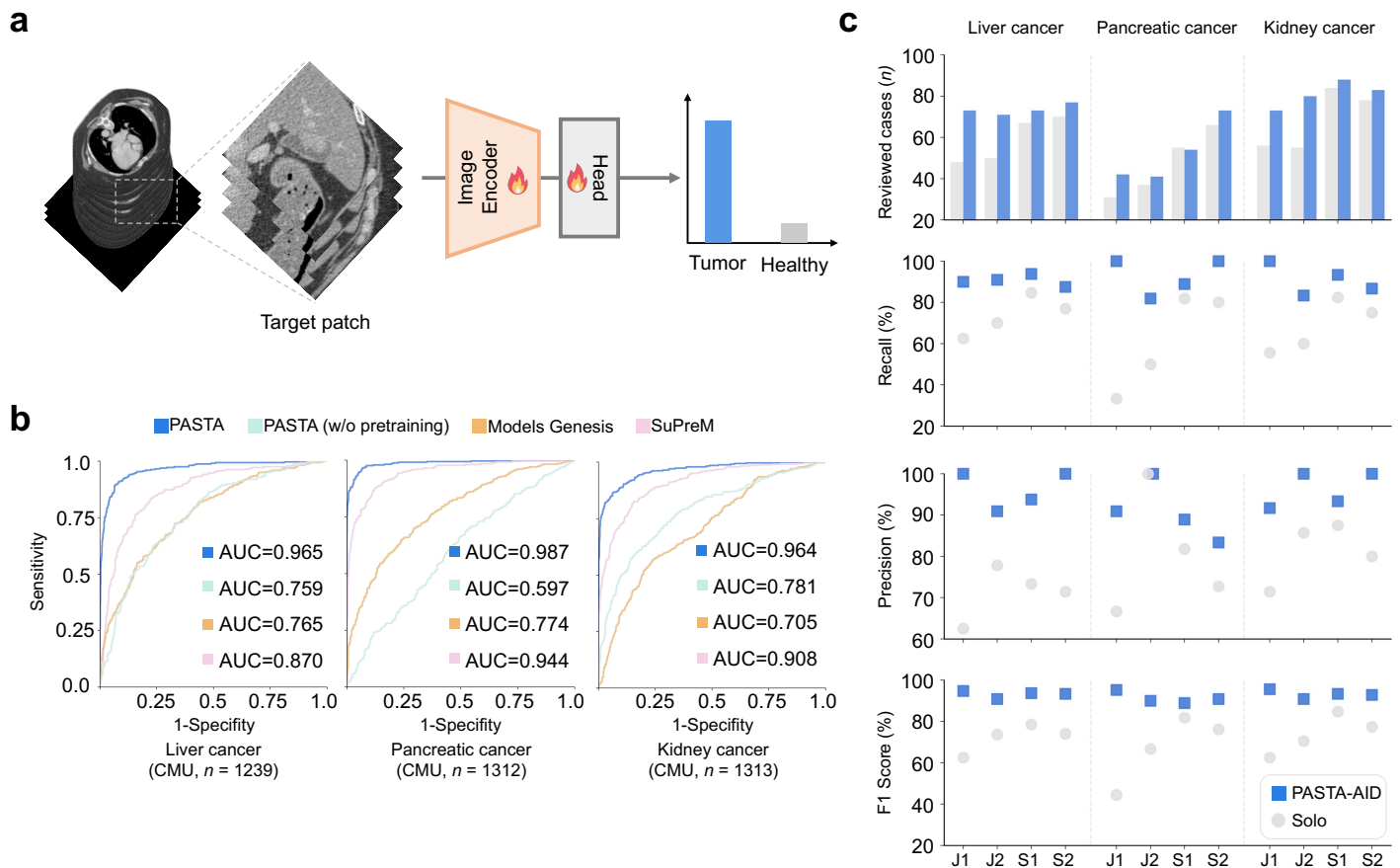


Fig. 2 | Performance in Non-contrast CT Tumor Identification. **a**, Workflow of the classification tasks: target patches were cropped and fed into the encoder, followed by an MLP head to predict class probabilities. **b**, Performance of different models in non-contrast CT tumor screening, measured by AUC. **c**, Results of simulated high-workload non-contrast CT tumor screening within a fixed 30-minute reading window, with and without PASTA-AID assistance. J1 and J2 denote the two junior radiologists, and S1 and S2 denote the two senior radiologists.

For this task, we collected 323 liver tumor cases with 916 matched healthy scans, 338 pancreatic tumor cases with 974 matched healthy scans, and 340 kidney tumor cases with 973 matched healthy scans at the First Hospital

of CMU. Multi-layer perceptrons (MLPs) were added after the encoder for classification (Fig. 2a). Further details of the non-contrast CT tumor identification experiments and their performance are provided in the Methods and Supplementary Table 2. In this task, PASTA achieved AUC values ranging from 0.964 to 0.987 across the three cancer types, outperforming both the PASTA model without pre-training and other pre-trained models, including Models Genesis and SuPreM. PASTA's accuracy and AUC scores consistently surpassed the second-best models.

In the subsequent clinical trial under the screening-aid scenario, two junior and two senior radiologists each performed tumor screening tasks for the liver, pancreatic, and kidney under both unaided (solo) and PASTA-AID – assisted conditions. In each round, radiologists were given a fixed 30-minute window to evaluate as many cases as possible from a randomized cohort of 180 non-contrast CT scans, comprising 30 scans with pathologically confirmed organ-specific tumors and 150 scans of normal organs. In the assisted mode, the PASTA-AID system provided probabilistic predictions of tumor occurrence in the target organ, which radiologists could directly incorporate into their decision-making.

With PASTA-AID assistance, both junior and senior radiologists achieved substantial performance gains across all tumor types (Fig. 2c, Supplementary Table 2). The most pronounced recall improvement was observed for pancreatic tumors, where average recall increased from 61.3% to 92.7%, resulting in an F1 score increase from 67.3% to 91.3%. The largest precision gain was seen for kidney tumors, with precision rising from 81.2% to 96.2%, alongside a recall increase from 68.2% to 90.8% and an F1 score improvement from 73.8% to 93.2%. Liver tumors also showed consistent enhancements, with precision improving from 71.3% to 96.2% and recall from 73.5% to 90.5%, yielding an F1 score increase to 93.2%. When averaged across all cancer types and radiologists, PASTA-AID boosted recall by 23.7%, precision by 16.8%, and F1 score by 21.4%.

In addition to enhancing diagnostic accuracy, PASTA-AID also improved efficiency in the time-limited screening task. The number of cases reviewed within 30 minutes increased by 25.1% for liver, 11.1% for pancreatic, and 18.7% for kidney cancers compared with unaided reading. Together, these findings demonstrate

that PASTA-AID not only enhances accuracy and efficiency in high-volume screenings but also enables junior radiologists to approach expert-level diagnostic performance on challenging non-contrast CT tumor identification tasks.

2.2 Full-Data Lesion Segmentation

We then evaluated PASTA’s lesion segmentation performance using the full set of annotated data and sufficient training steps. Publicly available datasets with lesion mask annotations were prioritized, including the MSD²⁵ dataset (lung tumor, liver tumor, pancreatic tumor and cyst, colon cancer) and the KiTS23²⁶ dataset (kidney tumor and cyst). For lesion types lacking publicly available datasets with annotated masks, we collected and annotated additional data from the First Hospital of CMU, covering gallbladder cancer, esophageal cancer, gastric cancer, bladder cancer, bone metastasis, liver cysts, gallstones, and kidney stones, resulting in a total of 1,535 scans.

To assess PASTA’s performance, we compared it with other FM models (Models Genesis²⁰ and SuPerM²²) and established segmentation frameworks (nnUNet²³ and Universal²⁴). Details regarding the segmentation tasks, experimental setup, and performance are provided in the Methods section, Extended Table 4, and Supplementary Table 3.

Across all 15 lesion segmentation tasks, PASTA consistently outperformed other pretrained models, achieving DSC ranging from 0.433 to 0.814 (Fig. 3a, b, and Supplementary Table 3), except for gallstone segmentation, where it performed slightly below nnUNet. In seven tumor segmentation tasks, PASTA significantly surpassed the next best-performing model, with performance improvements as follows: lung tumor (+1.9%, $P = 0.018$), liver tumor (+2.3%, $P < 0.001$), pancreatic tumor (+1.9%, $P = 0.010$), esophageal cancer (+3.7%, $P = 0.004$), gastric cancer (+4.6%, $P = 0.004$), kidney tumor (+1.4%, $P < 0.001$), and bone metastasis (+4.4%, $P = 0.020$). Notably, for tumors that typically exhibit lower segmentation performance, such as gastric cancer and bone metastasis, PASTA demonstrated more pronounced improvements in segmentation accuracy.

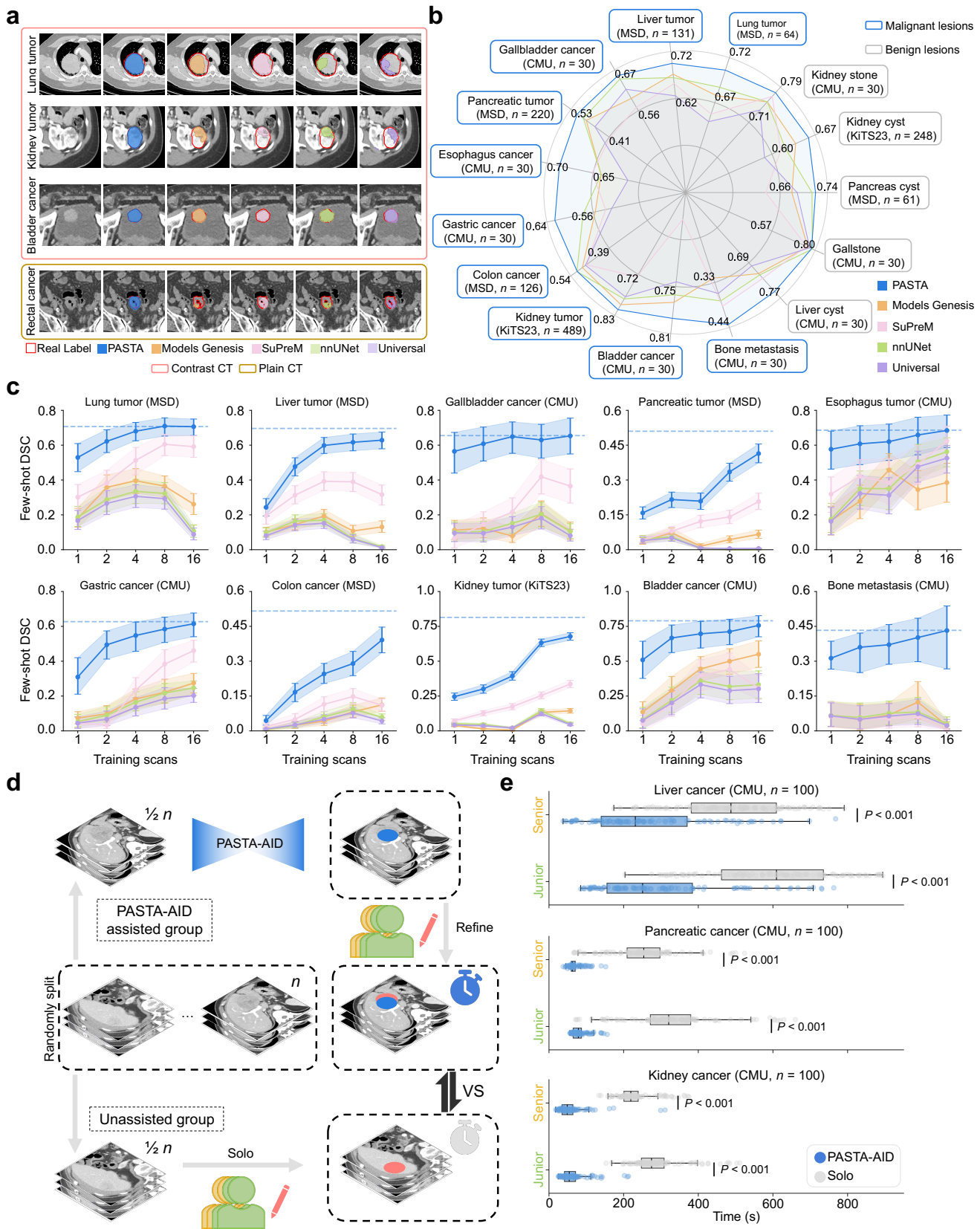


Fig. 3 | Comparison on Lesion Segmentation. a, Example images of lesion segmentation results from various

models. **b**, Comparison of model performance in lesion segmentation with sufficient data, measured by DSC. **c**, Lesion segmentation performance of models under few-shot settings, with blue dashed lines indicating PASTA's full-data training results. Error bands denote 95% confidence intervals. **d**, Lesion segmentation reader study design. Radiologists reviewed randomly assigned scans under PASTA-AID-assisted or unassisted conditions. **e**, Lesion mask annotation time of radiologists with different levels of experience, with and without PASTA-AID assistance. Box plots show the median (center line), interquartile range (IQR, box limits represent 25th and 75th percentiles), and whiskers extending to $1.5 \times \text{IQR}$; outliers are shown as individual points. Report time differences between groups were assessed using a linear mixed-effects model with doctor as a random intercept, and corresponding p-values are reported.

2.3 Few-Shot Lesion Segmentation

An essential capability of foundation models is label-efficient learning and effective transfer learning, which are particularly valuable for analyses under conditions of limited data availability. For label-efficiency tests, we used the same datasets as for the full-data supervised lesion segmentation task. In scenarios with limited training data ($K \in \{1, 2, 4, 8, 16\}$) and a small number of training iterations (2,000 iterations), PASTA significantly outperformed all baseline models, achieving segmentation performance improvements ranging from 0.025 to 0.463 (Fig. 3c).

Notably, under extremely limited data conditions ($n \leq 2$), PASTA demonstrated remarkable performance for certain cancers. For gallbladder cancer ($n=2$), PASTA achieved a DSC of 0.608, significantly outperforming SuPerM (46.3%, $P < 0.001$), and approaching the performance of models trained on the full dataset (DSC of 0.654). Similarly, for bladder cancer ($n=2$), PASTA achieved a DSC of 0.667, outperforming Models Genesis by +37.7% ($P < 0.001$), and approaching the full dataset performance (DSC of 0.790) (Fig. 3c and Supplementary Table 3). These findings highlight PASTA's ability to achieve high segmentation accuracy with minimal training data, making it especially effective for rare lesion types with limited annotated data.

2.4 Clinical efficiency of PASTA-AID in segmentation

In the retrospective clinical trial under the diagnosis-aid scenario, the PASTA-AID system, incorporating a target lesion segmentation model that automatically delineates lesions while allowing radiologists to refine the masks as needed, demonstrated substantial improvements in workflow efficiency (Fig. 3d,e and Supplementary Table 4). In this study, two junior and two senior radiologists segmented 50 cases for each cancer type (liver, pancreatic,

and kidney), both with and without PASTA-AID assistance. For senior radiologists, the average per-case lesion segmentation time was significantly reduced across the three cancers with PASTA-AID compared with unaided reading, with reductions up to 74.5%. Among junior radiologists, the reduction was even greater, reaching 78.2%.

In the evaluation of PASTA-AID's enabling effect on junior radiologists, marked improvements were observed in their lesion segmentation performance with PASTA-AID assistance (Supplementary Table 4). Specifically, when benchmarked against the gold-standard annotations created by senior radiologists, the segmentations produced by juniors with assistance showed markedly higher concordance, with an increase in Dice similarity of 11.8% to 12.2%. This improvement indicates that PASTA-AID substantially narrowed the performance gap between junior and senior readers, enabling less-experienced radiologists to achieve segmentation quality approaching expert-level annotations.

2.5 Structured Lesion Report Generation

Linguistic descriptions of lesion imaging characteristics are vital for understanding and evaluating lesion properties. To assess PASTA's capability in generating structured reports, we followed the structured report format of PASTA-Gen and annotated 1,535 scans corresponding to 15 lesion types (Fig. 4a, Methods, Extended Data Table 1, 4). The structured report generation task was formulated as a multi-class classification problem for each attribute. For PASTA, the encoder and MLP components were fine-tuned for this task, while for Models Genesis and SuPreM, their encoders were retained and supplemented with an MLP classifier.

Systematic evaluation revealed that PASTA outperformed competing models in generating structured reports across all lesion types. Both F1 scores and accuracy metrics surpassed those of the next best-performing models (Fig. 4b and Supplementary Table 6), except for the invasion attribute, where PASTA's performance was on par with SuPreM. Compared to the next best-performing model, PASTA demonstrated significant improvements in both accuracy and F1-score, including +6.0% ($P < 0.001$) and +3.9% ($P = 0.017$) for shape, +3.7% ($P < 0.001$) and 4.0% ($P < 0.001$) for density, +3.2% ($P < 0.001$) and +4.3% for heterogeneity ($P < 0.001$), and +2.8% ($P < 0.001$)

and +3.8% for surface ($P < 0.001$).

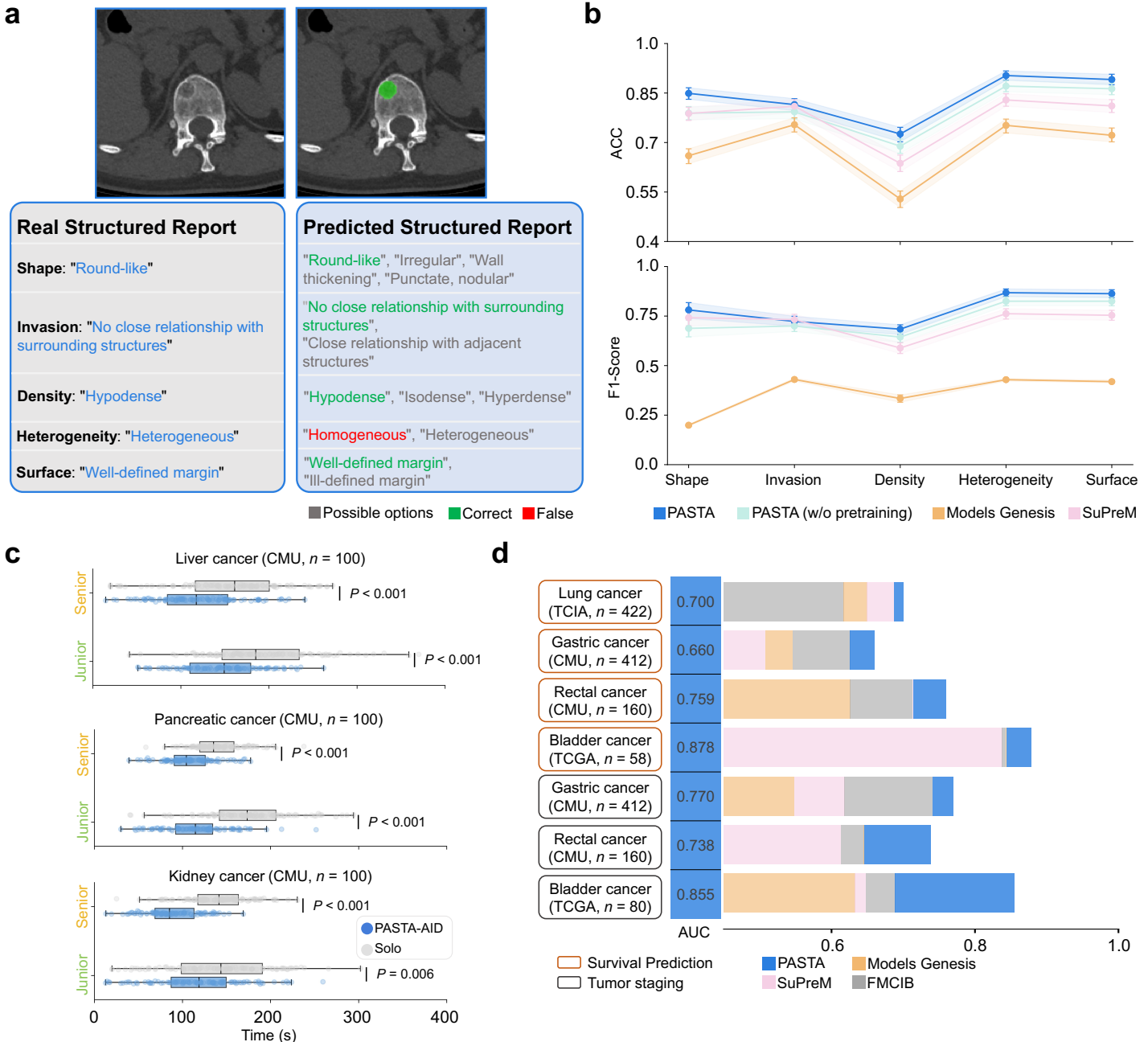


Fig. 4 | Comparison on Structured Lesion Report Generation. **a**, Example of real and predicted lesion structure reports for bone metastasis generated by PASTA. **b**, Comparison of Accuracy (ACC) and F1-scores for five structured report attributes across different models. Error bands denote 95% confidence intervals. **c**, Reporting time of radiologists with different levels of experience, under conditions with and without PASTA-AID assistance. Box plots show the median (center line), interquartile range (IQR, box limits represent 25th and 75th percentiles), and whiskers extending to $1.5 \times$ IQR; outliers are shown as individual points. Report time differences between groups were assessed using a linear mixed-effects model with doctor as a random intercept, and corresponding p-values are reported. **d**, Performance of models in tumor staging and survival prediction across various tumor types.

In the retrospective clinical trial, the PASTA-AID system automatically generated draft structured lesion reports using the same encoder-classifier configuration as in the report generation task and allowed radiologists to edit and finalize them. This approach further improved reporting efficiency, reducing report generation time by 15.7%-36.5% across tumor types and radiologist experience levels (Fig. 4c and Supplementary Table 4). For junior radiologists, PASTA-AID assistance also led to higher concordance with senior radiologists' reports compared with solo reading; however, these improvements were not statistically significant (Supplementary Table 5).

2.6 Tumor Staging and Survival Predictions

For frontline clinicians, the ability to perform tumor staging and survival predictions is crucial in clinical applications. We tested PASTA's performance in tumor staging prediction for three types of tumors (gastric cancer, rectal cancer, and bladder cancer) and survival prediction for four types of tumors (lung cancer, gastric cancer, rectal cancer, and bladder cancer). For the tumor staging prediction task, we compared the models' ability to differentiate between relatively early and late stages of tumors (gastric cancer: stage I-II vs. stage III-IV; rectal cancer: stage I-III vs. stage IV; bladder cancer: stage I-II vs. stage III-IV). For the staging task, we utilized the TCGA-BLCA²⁷ public dataset (bladder cancer) and the CMU dataset (gastric cancer and rectal cancer). In survival prediction, considering the practical aspects of survival data collection, we compared the models' ability to distinguish between short and long tumor-related overall survival (OS) durations (lung tumor: OS < 2 yrs vs. OS \geq 2 yrs; gastric cancer: OS < 2 yrs vs. OS \geq 2 yrs; rectal cancer: OS < 3 yrs vs. OS \geq 3 yrs; bladder cancer: OS < 3 yrs vs. OS \geq 3 yrs). For the survival task, we used the TCIA²⁸ public dataset (lung cancer), TCGA-BLCA²⁷ public dataset (bladder cancer), and the CMU dataset (gastric cancer and rectal cancer). In evaluating model performance, we specifically included the FMCIB²¹ model, a CT pre-trained model that places greater emphasis on clinical phenotype-related biomarkers, for comparison (Methods). The results revealed that PASTA achieved outstanding performance in these tasks (Fig.4d and Supplementary Table 7). In the tumor staging tasks, PASTA's predictions

achieved an AUC of 0.770–0.855, with significant improvements over the next best-performing model: +0.029 in gastric cancer ($P = 0.031$), +0.092 in rectal cancer ($P = 0.031$), and +0.166 in bladder cancer ($P = 0.031$). Meanwhile, for the survival prediction tasks, PASTA reached an AUC of 0.660–0.878, outperforming the next best-performing model by +0.034 in gastric cancer ($P = 0.031$) and +0.045 in rectal cancer ($P = 0.094$).

2.7 Efficient Oncology Transfer Learning Across Modalities

Foundation models should excel in rapid transfer learning, allowing efficient adaptation to new imaging modalities. While PASTA was pre-trained on CT data, MRI is a widely used 3D imaging modality with both similarities and complementarities to CT. To evaluate PASTA's label-efficient transfer performance, we tested it on MRI brain tumor and liver tumor datasets (Methods and Extended Table 4). Under limited training data conditions ($K \in \{1, 2, 4, 8, 16\}$) with only 2,000 training iterations, PASTA consistently outperformed other models, demonstrating superior generalization. In the cross-domain MRI brain tumor dataset, which contained head images not included in PASTA's training data, the model achieved a DSC of 0.504 at $n=16$, significantly exceeding the second-best model, SuPreM, which scored 0.468 ($P < 0.001$). Similarly, in the cross-domain MRI liver tumor dataset—comprising chest and abdominal images that were present in PASTA's training data—the model attained a DSC of 0.603 at $n=16$, outperforming SuPreM by +13.4% ($P < 0.001$) (Supplementary Table 1).

Overall, these findings highlight PASTA's exceptional capacity for efficient cross-modality transfer learning compared to other CT-pretrained models. We hypothesize that this may reflect PASTA's ability to effectively differentiate between normal and abnormal tissues across diverse imaging modalities.

3 Systematic Evaluation of Synthetic Data Quality

The realism of generated images is a critical determinant of the utility of synthetic data. Accordingly, at the outset of the study, we conducted a systematic evaluation of both the image realism and text-image consistency of PASTA-Gen outputs (Extended Data Table 4). A panel of four radiologists assessed the realism of PASTA-Gen – generated images and the accuracy of their paired structured text descriptions (Fig. 5a).

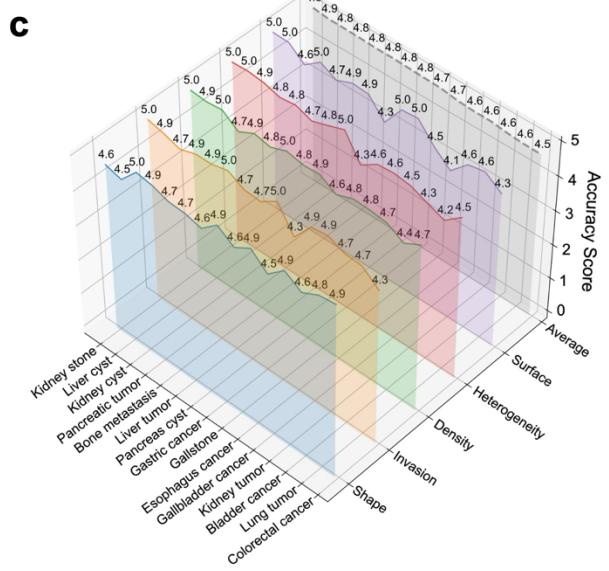
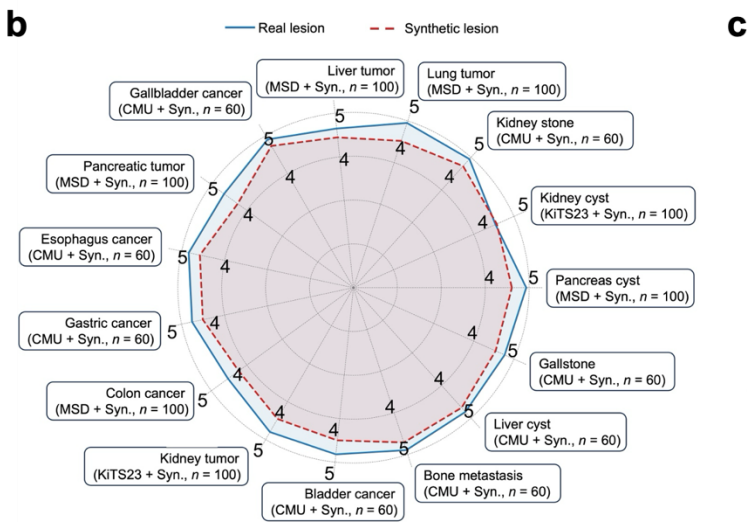
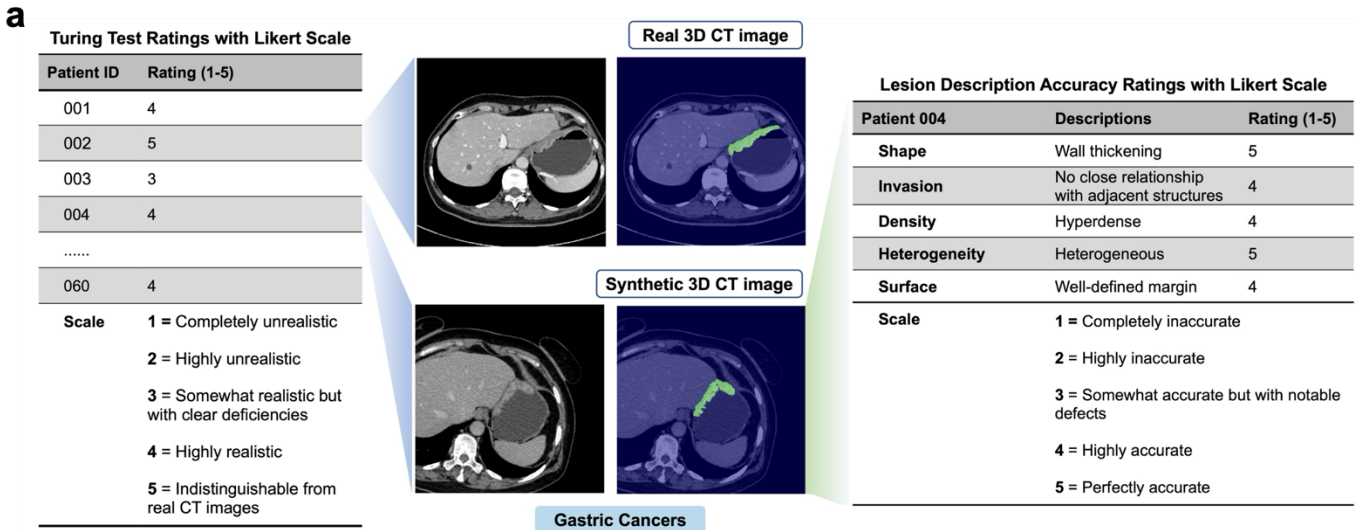


Fig. 5 | Generated Image and Description Accuracy Evaluation for PASTA-Gen. **a**, Illustration of Turing test ratings with Likert scale and lesion description accuracy ratings with Likert scale. **b**, Average Turing test scores of real and synthetic lesions. **c**, Average accuracy scores of structured report descriptions for each lesion type.

For image realism, real and generated data for each lesion type were mixed in a 1:1 ratio (Methods and Extended Data Table 5), resulting in a combined dataset of 1,180 cases. All four radiologists performed a blind Turing test, rating each sample on a scale of 1 (completely unrealistic) to 5 (indistinguishable from real CT images). The results showed that radiologists assigned PASTA-Gen's simulated data an average score ranging from 4.23 to 4.73 (Fig. 5b), with most ratings above 4. This indicates that the majority of data simulated by PASTA-Gen consistently met the "highly realistic" rating standard. Notably, for kidney cysts, the simulated data achieved an average score of 4.57, slightly surpassing the real data score of 4.54.

For the lesion descriptions, PASTA-Gen generated 50 images with corresponding reports for each of the 15 lesion types, resulting in a total of 750 image-mask-text pairs. The four radiologists evaluated the alignment between descriptions and five key attributes—shape, density, heterogeneity, surface characteristics, and adjacency to surrounding organs—using a scale from 1 (completely inaccurate) to 5 (perfectly accurate). Across all lesion types, the average consistency scores ranged from 4.54 to 4.93. Cysts and calcifications exhibited exceptionally high text-image consistency, while tumor-like lesions also demonstrated a match level exceeding the "highly accurate" standard (Fig. 5c).

Taken together, these results demonstrate that PASTA-Gen generates images that are nearly indistinguishable from real CT scans and produces structured text descriptions that closely align with radiological features, thereby providing a reliable foundation for downstream model training and clinical evaluation.

Discussion

This study introduces PASTA, a novel 3D-radiology foundation model for pan-tumor analysis across multiple cancer types. A key contribution of this work is the development of PASTA-Gen, a generative model capable of synthesizing realistic lesions across ten organs and fifteen lesion types. Utilizing PASTA-Gen, we assembled the PASTA-Gen-30K dataset, comprising 30,000 synthetic 3D-CT scans with corresponding pixel-level lesion masks and structured reports. The two-stage pretraining paradigm, focusing on semantic segmentation and vision-language alignment, enabled PASTA to effectively leverage this extensive synthetic dataset and thereby overcome traditional data scarcity and privacy constraints. Comprehensive evaluations demonstrated that PASTA not only outperforms existing models in lesion segmentation and few-shot learning scenarios but also exhibits robust generalizability across diverse datasets and imaging modalities, including MRI. Additionally, PASTA excels in downstream tasks such as tumor detection in non-contrast CT scans, tumor staging, survival prediction, and structured report generation. Beyond algorithmic performance, we further translated PASTA into a clinical

decision support system, PASTA-AID, and validated it through a retrospective clinical trial. The trial demonstrated significant improvements in diagnostic efficiency, reporting accuracy, and physician-AI collaboration, underscoring the model's real-world applicability. These findings highlight PASTA's potential to enhance clinical diagnostics and prognostics, facilitate personalized treatment planning, and support a wide range of oncology research applications.

PASTA distinguishes itself from existing AI-driven imaging models through its comprehensive pan-tumor approach and the utilization of synthetic training data. Traditional models like Models Genesis²⁰, FMCIB²¹, and SuPreM²² focus on specific cancer types or require large annotated datasets, limiting their scalability. While FMCIB distinguishes lesions, it lacks fine-grained annotations. SuPreM suffers from narrow tumor type coverage and imprecise annotations, restricting its generalizability. In contrast, PASTA leverages the PASTA-Gen-30K synthetic dataset to encompass a broader spectrum of tumor types and organ systems, effectively addressing the data scarcity issue inherent in rare cancers.

First and foremost, by generating a large volume of publicly available, precisely controlled image-text pairs, PASTA-Gen itself provides a groundbreaking solution to the chronic shortage of real-world datasets with pixel-level lesion masks and comprehensive imaging reports. Manual annotation is extremely time-consuming and resource-intensive²⁹, and privacy regulations further restrict the sharing of patient data³⁰. High-quality synthetic data not only avoids these barriers but also provides new opportunities for researchers and clinicians to apply advanced computational methods and translational applications without compromising patient confidentiality.

Second, large-scale imaging foundation models—particularly those spanning multiple organs and tumor types—are exceedingly rare, largely due to the scarcity of annotated data. Yet biological commonalities among different malignancies across organ systems suggest that a unified model can yield powerful insights, as evidenced by breakthroughs in pathology^{31,32} and molecular biology research³³. By systematically simulating tumors across ten organs, PASTA is the first to establish a truly pan-tumor 3D imaging foundation model, thus overcoming

limitations posed by fragmented real-world datasets. Moreover, while models like nnUNet²³ and Universal²⁴ have set benchmarks in lesion segmentation, PASTA has consistently achieved higher DSC across all evaluated tumor types, demonstrating superior segmentation accuracy and reliability.

Lastly, the pan-tumor nature of PASTA translates into tangible benefits for a variety of downstream tasks, including few-shot learning, which remains one of the most pressing challenges in medical imaging³⁴. Many institutions, especially those focusing on specific or rare tumor subtypes, often can only gather minimal datasets, limiting their ability to train robust models. PASTA addresses this gap by maintaining high segmentation accuracy with as few as one or two labeled cases, thereby substantially reducing the burden of large-scale data collection and annotation. This advantage is particularly impactful for research centers or clinical settings with constrained resources, where even a handful of reliable training samples can yield meaningful results. Beyond few-shot learning, PASTA excels in structured report generation, staging, survival prediction, and other tasks, consistently outperforming established models. The integration of PASTA into the PASTA-AID system further extends these advantages into daily radiology practice. In simulated non-contrast CT screening tasks, PASTA-AID enabled radiologists to achieve 11.1%-25.1% higher screening efficiency, 17.0%-31.4% higher recall, and 10.5%-24.9% higher precision under time-limited, high-workload conditions, underscoring its potential to alleviate diagnostic burden in real-world settings. In the diagnostic-aid tasks, segmentation time was reduced by up to 78.2%, reporting efficiency increased by up to 36.5%, and junior radiologists showed markedly enhanced concordance with the gold-standard annotations of senior radiologists. Importantly, because this retrospective simulated trial was conducted in a large academic medical center, the results also illustrate PASTA-AID's role in supporting less-experienced radiologists by narrowing the performance gap with senior experts. Beyond large hospitals, the same capability could be extended to smaller regional hospitals or resource-constrained institutions, where experienced radiologists are scarce. In such contexts, PASTA-AID may not only enhance individual diagnostic accuracy but also contribute to raising the overall standard of oncological care at the societal level. Taken together,

these capabilities position PASTA as a unified, highly adaptable solution that outperforms specialized models—paving the way for broader adoption of AI-driven oncological imaging analysis.

Despite these promising outcomes, several limitations merit attention. First, although the synthetic data generation pipeline was carefully validated through radiologist assessments, artificial lesions may still exhibit subtle deviations from real-world complexity. Second, the model’s performance in rare tumor subtypes or atypical lesion presentations requires further validation with clinically acquired data. Lastly, while we integrated multi-phase CT scans from different institutions, additional data from broader patient populations would further enhance the model’s robustness and mitigate potential biases introduced by specific scanners or patient demographics.

In conclusion, the release of PASTA and PASTA-Gen-30K represents a significant advancement in the development of pan-tumor foundation models, effectively addressing key challenges related to data scarcity, privacy, and model generalizability. By leveraging synthetic training data, PASTA not only enhances tumor screening and lesion annotation performance but also extends its utility to a broad range of downstream clinical tasks. Through the PASTA-AID system, we further provide direct evidence of its clinical translational value, demonstrating meaningful improvements in efficiency, accuracy, and support for physicians. Moving forward, future research should focus on integrating additional imaging modalities, refining synthetic data generation to capture more complex clinical variations, and conducting extensive real-world validations across diverse populations. As AI-driven medical imaging continues to evolve, our work lays the foundation for developing more generalized, data-efficient, and clinically impactful models.

Reference

1. Bray, F., *et al.* Global cancer statistics 2022: GLOBOCAN estimates of incidence and mortality worldwide for 36 cancers in 185 countries. *CA: a cancer journal for clinicians* **74**, 229-263 (2024).
2. Kleeff, J. & Ronellenfitsch, U. AI and imaging-based cancer screening: getting ready for prime time. *Nature medicine* **29**, 3002-3003 (2023).
3. Cao, K., *et al.* Large-scale pancreatic cancer detection via non-contrast CT and deep learning. *Nature medicine* **29**, 3033-3043 (2023).
4. Ardila, D., *et al.* End-to-end lung cancer screening with three-dimensional deep learning on low-dose chest computed tomography. *Nature medicine* **25**, 954-961 (2019).
5. McKinney, S.M., *et al.* International evaluation of an AI system for breast cancer screening. *Nature* **577**, 89-94 (2020).
6. Preetha, C.J., *et al.* Deep-learning-based synthesis of post-contrast T1-weighted MRI for tumour response assessment in neuro-oncology: a multicentre, retrospective cohort study. *The Lancet Digital Health* **3**, e784-e794 (2021).
7. Lipkova, J., *et al.* Artificial intelligence for multimodal data integration in oncology. *Cancer cell* **40**, 1095-1110 (2022).
8. Moor, M., *et al.* Foundation models for generalist medical artificial intelligence. *Nature* **616**, 259-265 (2023).
9. Zhang, S. & Metaxas, D. On the challenges and perspectives of foundation models for medical image analysis. *Medical image analysis* **91**, 102996 (2024).
10. Brown, T., *et al.* Language models are few-shot learners. *Advances in neural information processing systems* **33**, 1877-1901 (2020).
11. Acosta, J.N., Falcone, G.J., Rajpurkar, P. & Topol, E.J. Multimodal biomedical AI. *Nature Medicine* **28**, 1773-1784 (2022).
12. Rajpurkar, P. & Topol, E.J. A clinical certification pathway for generalist medical AI systems. *The Lancet* **405**, 20 (2025).
13. Chen, R.J., *et al.* Towards a general-purpose foundation model for computational pathology. *Nature Medicine* **30**, 850-862 (2024).
14. Wang, X., *et al.* A pathology foundation model for cancer diagnosis and prognosis prediction. *Nature* **634**, 970-978 (2024).
15. Hua, S., Yan, F., Shen, T., Ma, L. & Zhang, X. Pathoduet: Foundation models for pathological slide analysis of H&E and IHC stains. *Medical Image Analysis* **97**, 103289 (2024).
16. Lei, W., Xu, W., Li, K., Zhang, X. & Zhang, S. MedLSAM: Localize and segment anything model for 3D CT images. *Medical Image Analysis* **99**, 103370 (2025).
17. Wang, G., *et al.* Mis-fm: 3d medical image segmentation using foundation models pretrained on a large-scale unannotated dataset. *arXiv preprint arXiv:2306.16925* (2023).
18. Wald, T., *et al.* Revisiting MAE pre-training for 3D medical image segmentation. *arXiv preprint arXiv:2410.23132* (2024).
19. Jiang, Y., *et al.* Anatomical invariance modeling and semantic alignment for self-supervised learning in 3d medical image analysis. in *Proceedings of the IEEE/CVF International Conference on Computer Vision* 15859-15869 (2023).
20. Zhou, Z., Sodha, V., Pang, J., Gotway, M.B. & Liang, J. Models genesis. *Medical image analysis* **67**, 101840 (2021).
21. Pai, S., *et al.* Foundation model for cancer imaging biomarkers. *Nature machine intelligence* **6**, 354-367 (2024).
22. Li, W., Yuille, A. & Zhou, Z. How Well Do Supervised 3D Models Transfer to Medical Imaging Tasks? in *The Twelfth International Conference on Learning Representations*.
23. Isensee, F., Jaeger, P.F., Kohl, S.A., Petersen, J. & Maier-Hein, K.H. nnU-Net: a self-configuring method for deep learning-based biomedical image segmentation. *Nature methods* **18**, 203-211 (2021).
24. Liu, J., *et al.* Clip-driven universal model for organ segmentation and tumor detection. in *Proceedings of the IEEE/CVF International Conference on Computer Vision* 21152-21164 (2023).
25. Antonelli, M., *et al.* The medical segmentation decathlon. *Nature communications* **13**, 4128 (2022).
26. Heller, N., *et al.* The state of the art in kidney and kidney tumor segmentation in contrast-enhanced CT imaging:

Results of the KiTS19 challenge. *Medical image analysis* **67**, 101821 (2021).

- 27. Kirk, S., *et al.* The Cancer Genome Atlas Urothelial Bladder Carcinoma Collection (TCGA-BLCA)(Version 8)[Data set]. *The Cancer Imaging Archive* **10**, K9 (2016).
- 28. Aerts, H., *et al.* Data From NSCLC-Radiomics (version 4)[Data set]. *The Cancer Imaging Archive* (2014).
- 29. Aljabri, M., AlAmir, M., AlGhamdi, M., Abdel-Mottaleb, M. & Collado-Mesa, F. Towards a better understanding of annotation tools for medical imaging: a survey. *Multimedia tools and applications* **81**, 25877-25911 (2022).
- 30. Thapa, C. & Camtepe, S. Precision health data: Requirements, challenges and existing techniques for data security and privacy. *Computers in biology and medicine* **129**, 104130 (2021).
- 31. Arslan, S., *et al.* A systematic pan-cancer study on deep learning-based prediction of multi-omic biomarkers from routine pathology images. *Communications Medicine* **4**, 48 (2024).
- 32. Fu, Y., *et al.* Pan-cancer computational histopathology reveals mutations, tumor composition and prognosis. *Nature cancer* **1**, 800-810 (2020).
- 33. Chen, R.J., *et al.* Pan-cancer integrative histology-genomic analysis via multimodal deep learning. *Cancer Cell* **40**, 865-878. e866 (2022).
- 34. Pachetti, E. & Colantonio, S. A systematic review of few-shot learning in medical imaging. *Artificial intelligence in medicine*, 102949 (2024).

Method

1 Development of PASTA-Gen

PASTA-Gen is a lesion editing model designed to simulate lesions on scans of target organs with healthy anatomy.

To develop PASTA-Gen, we first constructed a universal structured lesion report template, followed by the collection and annotation of real lesion data as a reference set. Using this reference data and the structured template, we iteratively refined the model through close collaboration with radiologists, ensuring its clinical relevance and accuracy. Finally, a denoising network was incorporated to enhance the realism of the generated images (Figure 1. C).

1.1 Structured Lesion Report Template

Building on previous studies on structured radiology reporting³⁵, we synthesized insights from existing research and analyzed a large collection of in-house radiology reports across various disease types. While no universal standard currently exists, radiologists consolidated lesion descriptions for solid tumors into eight key attributes, including enhancement status, location, size, shape, density, heterogeneity, surface, and invasion. These attributes form a comprehensive and objective template for characterizing lesions, ensuring consistency and enabling generalization across diverse lesion types (Extended Data Table 1).

One of these attributes, "density," typically relies on assessments from multiple CT modalities. For instance, in contrast-enhanced CT scans, radiologists often integrate information from different imaging phases to provide a nuanced evaluation of a lesion's density. However, as our study focuses on developing a cross-phase CT analysis model, the concept of "density" in PASTA-Gen refers to a relative assessment within a single-phase CT image. Specifically, it captures the density of the lesion area relative to the surrounding normal tissues in the given phase. This approach enhances the model's adaptability in representing lesions with complex or variable densities.

1.2 Real Lesion Reference Data

To ensure comprehensive modeling and evaluation of synthetic lesion data, we developed a diverse reference

dataset encompassing 15 target lesion types across 10 organs. This dataset includes lesion segmentations and structured reports derived from both public sources and in-house data from the First Hospital of CMU (Extended Data Table 4). For instances with incomplete labels, two senior radiologists meticulously supplemented the missing information, ensuring the dataset's accuracy and clinical relevance. We reformat all CT scans so that the first axis points from right to left, the second from anterior to posterior, and the third from inferior to superior. We then resample the spacing in all directions to 1 mm using linear spline interpolation.

1.3 Modeling Process for PASTA-Gen

The development of PASTA-Gen involved a multidimensional statistical analysis of collected real reference lesions, combined with iterative feedback from experienced radiologists. This collaborative approach enabled us to systematically model the eight structured attributes outlined in our framework.

Lesion size distributions were statistically represented using a log-normal distribution across various axes, with random sampling used to generate realistic dimensions. Lesion shapes were modeled based on the specific morphological characteristics of each type, such as the round-like shape of liver cysts or the wall thickening observed in gastric cancer. These shape parameters ensure the model captures the clinical nuances of different lesions. Density attributes were linearly modeled with controlled variability, determined by calculating the intensity of normal tissues surrounding the lesion on target organ scans. The lesion density was then derived by sampling from these calculated differences, ensuring alignment with clinical observations. Heterogeneity attributes, including brightness deviation and texture features, were modeled based on radiologist input. For instance, heterogeneous density patterns were simulated to reflect clinical variability. For solid tumors in parenchymal organs like liver and kidney tumors, we emphasized the boundary between the tumor and surrounding tissues, controlling this characteristic by adjusting the degree of Gaussian blur applied to the tumor edges. For hollow organs such as those in the gastrointestinal or urinary systems, surface features were modeled to highlight serosal roughness and outer surface irregularities. Invasion was modeled based on whether the lesion

extended beyond the target organ into adjacent tissues. For benign lesions, invasion into surrounding organs was explicitly avoided to maintain consistency with clinical presentations. Each simulated lesion is accompanied by a corresponding structured report containing eight attributes, with each attribute reflecting one of its possible values (Extended Data Table 1). This comprehensive approach ensures that PASTA-Gen generates synthetic lesions with high fidelity and clinical relevance, capable of capturing the diverse characteristics of real-world lesions.

1.4 Collection and Preprocessing of Template CT Scans and Radiology Report

To ensure the diversity and scalability of PASTA-Gen, we collected an additional 10,767 in-house CT scans to serve as the template scan set, which include both contrast-enhanced and plain phases, covering various parts of the body, along with their corresponding radiology reports (Extended Data Table 2). We reformat all CT scans so that the first axis points from right to left, the second from anterior to posterior, and the third from inferior to superior. We then resample the spacing in all directions to 1 mm using linear spline interpolation. We use TotalSegmentator³⁶ to segment the standardized scans. This tool segments 104 classes of organs, encompassing all the organs for which PASTA-Gen simulates lesions.

For the template CT scans. Based on the presence of specific organs, we only retain the following three study types of CT scans: (1) Chorax CT: must include the T1 vertebra, left upper lobe of the lung, and right upper lobe of the lung, but not include the L5 vertebra. (2) Abdomen-pelvis CT: must include the T8 vertebra and the bladder but not include the T1 vertebra. (3) Thorax-abdomen-pelvis CT: must include the T1 vertebra, left upper lobe of the lung, and right upper lobe of the lung and the bladder (Extended Data Table 3). Next, we determine whether each selected CT scan is contrast-enhanced by evaluating the Hounsfield unit (HU) values of the aorta and inferior vena cava. If the average HU of both the aorta and inferior vena cava is less than 80, the scan is classified as non-contrast. Otherwise, it is classified as contrast-enhanced. Based on the diagnostic modalities typically used by radiologists for different types of lesions, we selected the appropriate scanning regions and modalities for

simulating each type of lesion (Supplementary Table 8).

To ensure that PASTA-Gen simulates target lesions on healthy organs, we implemented a filtering process based on the radiology report associated with each CT scan. For the target organ in each CT scan, the criteria for being classified as healthy are as follows: (1) the volume of the organ is larger than 4000 mm³, and (2) the corresponding radiology report impression does not mention the organ, as determined by keyword search. By applying these criteria, we ensure that only healthy organs are used for simulating lesions (Extended Data Table 4).

1.5 Details of Denoising Network

The denoising network in PASTA-Gen aims to optimize the initially synthesized lesions. This network is based on a 3D medical denoising diffusion probabilistic model (DDPM)^{37,38}, which involves adding random Gaussian noise to the original image and learning how to remove it. We leverage this property to eliminate unnatural parts of the simulated lesions. During the training phase, the input image size is 128×128×128. We concatenate the corresponding organ segmentation mask as the input condition for the model (Figure 1, Extended Figure 1). We set the total timesteps T to 1000 and utilize the L_1 loss to measure the difference between predicted and added noise. The model channel number is set to 16. We use an AdamW optimizer³⁹ with an initial learning rate of 1×10^{-4} and weight decay of 1×10^{-5} . We employ a total batch size of 8 across 4 NVIDIA GTX4090 GPUs. During the lesion generation stage, the initially simulated lesions are input into the denoising network for $t = 5$ optimization iterations. A sliding window approach is applied to ensure comprehensive and seamless optimization across the entire image volume.

2 Dataset Curation for PASTA-Gen-30K

Using PASTA-Gen, we simulated 2,000 instances for each of the 15 target lesion types, resulting in a dataset of 30,000 lesion image-mask-text pairs. Since the template scan set includes organ segmentation results generated by TotalSegmentator, the labels for the simulated images retain all 10 target organ labels alongside the lesion

labels, totaling 25 categories (Supplementary Table 9).

3 Details of PASTA Pretraining

The PASTA model leverages a 3D UNet⁴⁰ architecture for its encoder and decoder, with a three-layer MLP serving as the classification head. The encoder and decoder of the 3D UNet architecture each consist of five convolutional blocks. Each convolutional block is composed of two sub-blocks, and within each sub-block, there is a 3D convolution operation with a kernel size of $3 \times 3 \times 3$ and a stride of 1 along each dimension. Each convolution is followed by a 3D Instance Normalization^{41,42} activation function. In the encoder, each convolutional block is followed by a max pooling operation with a kernel size of $2 \times 2 \times 2$, while in the decoder, each block is followed by a transposed convolution operation with a stride of 2, which up-samples the spatial resolution. The MLP classification head consists of an input layer with 1024 channels, followed by two hidden layers with channel sizes of 512 and 256, and a final output layer mapping to the number of classes. Each intermediate layer is followed by a LeakyReLU activation function.

During the initial segmentation pretraining stage, we employed the nnUNet framework²³, which has demonstrated state-of-the-art performance across various biomedical image segmentation tasks^{43,44}. The training target is to segment all 25 categories in PASTA-Gen-30K. The training process used an initial learning rate of 1×10^{-2} and was conducted over 2,000 epochs, with each epoch comprising 250 iterations. Random cropping was applied to extract 3D patches of size $128 \times 128 \times 128$ voxels for training. The loss function combined Cross-Entropy Loss and Dice Loss⁴⁵, optimizing for both pixel-wise classification accuracy and volumetric overlap. Training was conducted with a total batch size of 16, distributed across 8 NVIDIA GTX 4090 GPUs.

In the second stage of lesion attribute classification pretraining, the 3D UNet component is frozen, and only the MLP connected to the encoder is trained. The training objective is to predict lesion attributes from the structured reports in the PASTA-Gen-30K dataset, including Shape, Density, Heterogeneity, Surface, and Invasion attributes. Each attribute comprises fixed categories: Shape (4 classes), Density (3 classes), and

Heterogeneity, Surface, and Invasion (2 classes each). The task is formulated as a multi-class classification problem. The initial learning rate is set to 1×10^{-3} , and the training runs for a total of 100,000 iterations. The loss function used is Cross-Entropy Loss. During training, patches of size $96 \times 96 \times 96$ voxels, centered on the lesion, are cropped and fed into the network to focus on the lesion region. Training was conducted with a total batch size of 64, distributed across 4 NVIDIA GTX 4090 GPUs.

4 Competing Methods and Baselines

We compare PASTA to 5 comparison approaches. Models Genesis²⁰ was a released model pretrained on 623 Chest CT scans in LUNA 2016⁴⁶. It utilized a 3D UNet architecture and employed a self-supervised learning approach by recovering the original sub-volumes of images from their transformed versions. SuPreM²² was pretrained in a supervised segmentation setting on the AbdomenAtlas 1.1 dataset⁴⁷ which comprises 9,262 CT volumes with detailed annotations of 25 anatomical structures and pseudo annotations for seven tumor types. SuPreM incorporates multiple backbone architectures, and we selected the 3D UNet model for evaluation as it demonstrated the best performance in SuPreM experimental results. FMCIB²¹ used a Resnet⁴⁸ as the backbone and was pretrained with a comprehensive dataset of 11,467 radiographic lesions in DeepLesion⁴⁹. It is tailored for cancer imaging biomarker discovery by contrasting volumes with and without lesions. nnUNet²³ and Universal²⁴ are both state-of-the-art frameworks for biomedical image segmentation.

5 Construction of PASTA-AID

To bridge algorithmic advances with clinical applicability, we developed PASTA-AID, a clinical decision support system built upon the PASTA foundation model. PASTA-AID was designed in close collaboration with radiologists to integrate seamlessly into existing workflows, aiming to reduce interpretation time and improve diagnostic consistency without replacing physicians' expertise.

5.1 System Design and Implementation

PASTA-AID was implemented in Python (v3.9.7) with an HTML-based interactive interface (built using Flask-

based rendering, matplotlib v3.10.0, seaborn v0.13.2, hiddenlayer v0.3). The system ingests NIfTI-format CT scans and leverages PASTA for tumor screening, lesion segmentation, and report generation (implemented with torch v2.2.0, SimpleITK v2.4.1, nibabel v5.3.2, numpy v2.2.2, pandas v2.2.3, Scikit-learn v1.6.1, scipy v1.15.1). Utility packages such as tqdm v4.66.4 and Requests v2.32.3 were used for progress monitoring and data handling. The interface displays three orthogonal CT views (axial, coronal, sagittal) and allows users to interactively scroll through slices. In the non-contrast CT screening setting, PASTA-AID outputs the estimated cancer probability for the target organ in addition to visual overlays. In the diagnosis setting, the system generates pixel-level lesion masks and structured radiology reports. Radiologists can refine both outputs: masks can be manually adjusted at the pixel level, and report items can be modified via selectable options.

5.2 Workflow Integration

PASTA-AID supports two primary clinical use cases: (1) screening-aid, enabling rapid tumor detection under time-limited non-contrast CT conditions; and (2) diagnosis-aid, performing detailed lesion segmentation and automatic structured reporting on contrast-enhanced CT. In both workflows, the system emphasizes collaboration with radiologists, ensuring that users remain the final decision-makers.

5.3 Validation Settings

The system was evaluated in a retrospective clinical trial (ChiCTR2500101081). Radiologists of varying experience levels interacted with PASTA-AID on a 24-inch 1080p display monitor, consistent with clinical reading environments. Performance was assessed under both screening-aid and diagnosis-aid settings, with metrics covering efficiency, accuracy, and inter-observer concordance. Detailed results are reported in the Results section.

6 Non-contrast CT Tumor Identification

Detecting tumors in non-contrast CT scans demonstrates the ability of models to identify subtle lesions, showcasing their potential for clinical applications. This study includes 3 tumor classification tasks and 3 tumor

segmentation tasks, focusing on liver cancer, pancreatic cancer, and kidney cancer. A total of 323 liver tumor scans with 916 healthy controls, 338 pancreatic tumor scans with 974 healthy controls, and 340 kidney tumor scans with 973 healthy controls were collected from the First Hospital of CMU. All CT scans are reoriented such that the first axis runs from right to left, the second from anterior to posterior, and the third from inferior to superior. The voxel spacing is then uniformly resampled to 1 mm in all directions using linear spline interpolation. For the tumor classification tasks, a conventional two-stage detection paradigm was adopted. This involved pre-extraction of target organs followed by classification of the extracted ROI volumes. TotalSegmentator was applied to segment the target organs in each scan, and the segmented regions were cropped with a 24-voxel margin in all directions. The cropped volumes were resized and padded to a uniform size of $128 \times 128 \times 128$ voxels. The PASTA model retained its encoder and MLP components, with the MLP's final layer adjusted to output two channels (non-cancer and cancer). Models Genesis and SuPreM retained their encoders, with a three-layer MLP appended, comprising two hidden layers (channel sizes of 512 and 256) and a final output layer with two channels; each intermediate layer was followed by a LeakyReLU activation function. The training process utilized the Adam optimizer on 4 NVIDIA GTX 4090 GPU with a total batch size of 32. The training was conducted with a base learning rate of 1×10^{-4} over 10000 iterations, with each epoch consisting of 250 iterations. Performance evaluation was conducted using the AUC metric with 5-fold cross-validation.

In the PASTA-AID experiment, an additional 60 tumor cases and 300 healthy organ scans were collected for each cancer type (liver, pancreas, and kidney) from the First Hospital of CMU. For each organ, the target region was first segmented using TotalSegmentator and then cropped with a 24-voxel margin in all directions to obtain the corresponding organ patch. The dataset was evenly divided between the PASTA-AID – assisted and unaided (solo) settings, ensuring no case overlap across conditions. Accordingly, for each cancer type, every radiologist was randomly assigned 30 tumor cases and 150 healthy cases in the solo setting, while the remaining cases of equal number were allocated to the PASTA-AID – assisted setting. In practice, each radiologist was instructed to

review as many cases as possible within a 30-minute session for each condition, rather than being required to complete the entire set. Two junior and two senior radiologists participated in the study, simulating real-world high-workload screening scenarios.

For the assisted setting, the corresponding PASTA-trained classification models were applied with 5-fold ensemble predictions, and the estimated malignancy probabilities were displayed to the radiologists. Performance was evaluated to quantify the benefit of PASTA-AID in accelerating tumor detection under high-throughput conditions, using three key metrics: 1) Recall: the proportion of true positives identified within 30 minutes relative to the total number of positive cases; 2) Precision: the proportion of true positives among all positive predictions within 30 minutes; 3) Workload throughput: the total number of cases reviewed by each radiologist within the time limit.

7 Full-Data Lesion Segmentation

From the lesion reference dataset, we constructed 15 lesion segmentation tasks (Extended Data Table 4), including MSD²⁵ dataset (lung tumor, liver tumor, pancreatic tumor and cyst, colon cancer) and the KiTS23²⁶ dataset (kidney tumor and cyst), as well as private scans from the First Hospital of CMU, covering liver cysts, gallbladder cancer, gallstones, esophageal cancer, gastric cancer, kidney stones, bladder cancer, and bone metastases. For the MSD Pancreas dataset, the original annotations for pancreatic cancer and pancreatic cysts shared the same label value. To address this, a senior radiologist manually differentiated and re-annotated them. For PASTA, Models Genesis, and SuPreM, we fine-tuned their encoder-decoder part using the nnUNet training framework with a base learning rate of 1×10^{-3} for 500 epochs, with each epoch comprising 250 iterations. Following the default nnUNet settings, the baseline nnUNet model was trained with a learning rate of 1×10^{-3} for 1,000 epochs. For the Universal model, we adhered to its standard configuration, training it with a learning rate of 1×10^{-4} for 2,000 epochs. Training random-crop patch-size is 128×128×128 voxel. All experiments were conducted on a single NVIDIA GTX 4090 GPU with a batch size of 2. The performances were evaluated in terms of the DSC using the

5-fold cross-validation.

8 Few-shot Lesion Segmentation

Few-shot learning is a common approach for evaluating the quality of features extracted by a pre-trained model and its ability to quickly adapt to new tasks with limited annotated data and transferring iterations. In this study, the few-shot lesion segmentation experiment was designed using the same 15 segmentation tasks and datasets as described in the fully supervised lesion segmentation section (Extended Data Table 4). To simulate few-shot settings, the number of labeled training scans per task was limited to $K \in \{1, 2, 4, 8, 16\}$, and the total training iterations for all models were capped at 2,000. For PASTA, Models Genesis, and SuPreM, we fine-tuned their UNet part using the nnUNet training framework with a base learning rate of 1×10^{-4} . The baseline nnUNet model was trained with a learning rate of 1×10^{-3} . For the Universal model, the learning rate is set to 1×10^{-4} . Training random-crop patch-size is $128 \times 128 \times 128$ voxel. All experiments were conducted on a single NVIDIA GTX 4090 GPU with a batch size of 2. The same 5-fold cross-validation splits used in the fully supervised setting were adopted, with K training samples randomly selected for each fold, repeated over five runs to ensure robustness. For the KiTS23 dataset, training samples were specifically chosen to ensure that each selected scan included both kidney tumors and kidney cysts.

9 Clinical efficiency of PASTA-AID in segmentation

For the segmentation-aid scenario, 200 patients were collected for each of the three cancer types (liver, pancreas, and kidney) from the First Hospital of CMU. Two junior and two senior radiologists participated in the study. In the PASTA-AID setting, a contrast-enhanced CT scan was randomly selected for each patient, and lesion masks were first generated by an ensemble of five PASTA-based models trained in the full-data lesion segmentation tasks using 5-fold cross-validation. Radiologists then refined these auto-generated masks to obtain the final annotations.

Segmentation time was defined as the period from loading the CT scan to completion of annotation, and was automatically recorded by a timer embedded in the system. The average time for junior and senior radiologists under both solo and PASTA-AID–assisted conditions was compared to evaluate the efficiency gain provided by the system.

To evaluate the empowering effect of PASTA-AID on less-experienced radiologists, segmentations produced by junior radiologists were compared with the reference standard, defined as the final annotations reviewed and confirmed by senior radiologists. Agreement between junior and senior annotations was quantified using the Dice similarity coefficient (DSC), which measures the spatial overlap between corresponding lesion masks.

10 Tumor Structure Report Generation

Evaluation of structured lesion reports utilized a reference dataset covering five attributes: shape, density, heterogeneity, surface, and invasion. The prediction tasks were framed as multi-label classification problems, requiring the model to predict an option for each attribute. CT scans are standardized by orienting the first axis from right to left, the second from anterior to posterior, and the third from inferior to superior. The voxel spacing is subsequently resampled to 1 mm in all directions using linear spline interpolation. For all tasks, regions of size $96 \times 96 \times 96$ voxels, centered on the lesion, are extracted and input into the network for classification. Fine-tuning was performed on PASTA, Models Genesis, and SuPreM models, each using a base learning rate of 1×10^{-4} . For Models Genesis and SuPreM, encoders were retained, with a three-layer MLP appended for attribute prediction. The training process involved Cross-Entropy Loss and the Adam optimizer with a total batch size of 32. Performance was assessed using the AUC metric and 5-fold cross-validation to ensure robust evaluation.

11 Tumor Staging and Survival Predictions

This study addresses seven tasks, including four cancer survival prediction tasks and three cancer staging tasks. The Lung1 dataset⁵¹ consists of 422 pretreatment CT scans from non-small cell lung cancer patients, annotated

with primary gross tumor volumes and overall survival information. Patients were classified into two categories: OS less than two years and OS of two years or more. The CMU gastric cancer dataset comprises 412 contrast-enhanced pretreatment abdominal CT scans from gastric cancer patients, annotated with tumor center points, survival data, and overall staging. The survival prediction task divides patients into OS less than two years and OS of two years or more, while staging distinguishes between stages I-II and III-IV. Similarly, the CMU rectal cancer dataset includes 160 contrast-enhanced pretreatment abdominal CT scans annotated with tumor center points, survival information, and overall staging, with tasks involving OS less than three years and OS of three years or more, as well as staging differentiation between stages I-III and stage IV. The TCGA-BLCA²⁷ dataset features 120 bladder cancer patients with imaging data and survival information, complemented by radiologist-annotated tumor center points. Survival prediction categorizes patients into OS less than three years and OS of three years or more, while staging separates stages I-II from III-IV. All CT scans are reformatted with the first axis oriented from right to left, the second from anterior to posterior, and the third from inferior to superior. The spacing in all directions is then resampled to 1 mm using linear spline interpolation. For all tasks, the FMCIB pipeline was adopted, which involves feature extraction from ROI regions centered on annotated tumor points for classification. Fine-tuning was performed on PASTA, Models Genesis, SuPreM, and FMCIB models, each using a base learning rate of 1×10^{-4} . For Models Genesis, SuPreM, and FMCIB models, encoders were retained, with a three-layer MLP appended for attribute prediction. The training process involved Cross-Entropy Loss and the Adam optimizer with a total batch size of 32. Performance was assessed using the AUC metric and 5-fold cross-validation to ensure robust evaluation.

12 Efficient Oncology Transfer Learning Across Modalities

A cross-modality evaluation was performed on two cancer segmentation tasks: (1) the MSD-Brain Tumors segmentation task²⁵, comprising 484 patients with FLAIR, T1w, T1gd, and T2w MRI scans. The segmentation targets included necrotic/active tumor regions and edema in gliomas. (2) The ATLAS⁵⁰ dataset, which includes

60 contrast-enhanced T1-weighted MRI scans of the liver from 60 patients with unresectable hepatocellular carcinoma (HCC), along with segmentation masks for the liver and liver tumors. In a few-shot learning setup, the number of labeled training scans was limited to $K \in \{1, 2, 4, 8, 16\}$, and total training iterations were capped at 2,000. PASTA, Models Genesis, and SuPreM models were fine-tuned using their UNet components within the nnUNet training framework, employing a base learning rate of 1×10^{-4} . The nnUNet baseline model was trained with a learning rate of 1×10^{-3} , while the Universal model used a learning rate of 1×10^{-4} . The training employed random-cropped patches of $128 \times 128 \times 128$ voxels. All experiments were performed on a single NVIDIA GTX 4090 GPU with a batch size of 2. The 5-fold cross-validation splits from the fully supervised setting were applied. The 5-fold cross-validation splits from the fully supervised setting were applied. For each fold, K training samples were randomly selected from the training set, and this process was repeated across five runs.

Data Availability

To advance oncology research, we release the PASTA-Gen-30K dataset, which consists of 30,000 synthetic 3D-CT scans with corresponding lesion masks and structured report descriptions at <https://huggingface.co/datasets/LWHYC/PASTA-Gen-30K>. The publicly available datasets used in this study can be accessed through the following sources: MSD (<http://medicaldecathlon.com/>); KiTS23 (<https://kits-challenge.org/kits23/>); Lung1 (<https://www.cancerimagingarchive.net/collection/nsclc-radiomics/>); TCGA-BLCA (<https://www.cancerimagingarchive.net/collection/tcga-blca/>); ATLAS (<https://atlas-challenge.u-bourgogne.fr/>). Structured report annotations for publicly available datasets, as well as lesion center point annotations for Lung1 and TCGA-BLCA, can be accessed at <https://github.com/LWHYC/PASTA>. Additional imaging data and associated clinical records were obtained from the First Hospital of China Medical University. Due to privacy regulations, these data cannot be publicly shared. This retrospective clinical study was reviewed and registered in the Chinese Clinical Trial Registry (<https://www.chictr.org.cn/>) under the registration number

ChiCTR2500101081.

Code Availability

The PASTA model, along with the full training and evaluation pipeline, is publicly available to facilitate further research and replication of our findings. The source code, model weights, and implementation details can be accessed at <https://github.com/LWHYC/PASTA>, ensuring accessibility for the broader clinical and scientific community.

Methods References

35. Nobel, J.M., van Geel, K. & Robben, S.G. Structured reporting in radiology: a systematic review to explore its potential. *European radiology*, 1-18 (2022).
36. Wasserthal, J., *et al.* TotalSegmentator: robust segmentation of 104 anatomic structures in CT images. *Radiology: Artificial Intelligence* **5**(2023).
37. Ho, J., Jain, A. & Abbeel, P. Denoising diffusion probabilistic models. *Advances in neural information processing systems* **33**, 6840-6851 (2020).
38. Yu, Y., *et al.* CT Synthesis with Conditional Diffusion Models for Abdominal Lymph Node Segmentation. *arXiv preprint arXiv:2403.17770* (2024).
39. Loshchilov, I. Decoupled weight decay regularization. *arXiv preprint arXiv:1711.05101* (2017).
40. Çiçek, Ö., Abdulkadir, A., Lienkamp, S.S., Brox, T. & Ronneberger, O. 3D U-Net: learning dense volumetric segmentation from sparse annotation. in *Medical Image Computing and Computer-Assisted Intervention-MICCAI 2016: 19th International Conference, Athens, Greece, October 17-21, 2016, Proceedings, Part II* 19424-432 (Springer, 2016).
41. Ulyanov, D. Instance normalization: The missing ingredient for fast stylization. *arXiv preprint arXiv:1607.08022* (2016).
42. Xu, B. Empirical evaluation of rectified activations in convolutional network. *arXiv preprint arXiv:1505.00853* (2015).
43. Tu, T., *et al.* Towards generalist biomedical AI. *NEJM A/1*, Aloa2300138 (2024).
44. Ma, J., *et al.* Unleashing the strengths of unlabelled data in deep learning-assisted pan-cancer abdominal organ quantification: the FLARE22 challenge. *The Lancet Digital Health* **6**, e815-e826 (2024).
45. Milletari, F., Navab, N. & Ahmadi, S.-A. V-net: Fully convolutional neural networks for volumetric medical image segmentation. in *2016 fourth international conference on 3D vision (3DV)* 565-571 (Ieee, 2016).
46. Setio, A.A.A., *et al.* Validation, comparison, and combination of algorithms for automatic detection of pulmonary nodules in computed tomography images: the LUNA16 challenge. *Medical image analysis* **42**, 1-13 (2017).
47. Li, W., *et al.* Abdomenatlas: A large-scale, detailed-annotated, & multi-center dataset for efficient transfer learning and open algorithmic benchmarking. *Medical Image Analysis* **97**, 103285 (2024).
48. He, K., Zhang, X., Ren, S. & Sun, J. Deep residual learning for image recognition. in *Proceedings of the IEEE conference on computer vision and pattern recognition* 770-778 (2016).
49. Yan, K., Wang, X., Lu, L. & Summers, R.M. DeepLesion: automated mining of large-scale lesion annotations and universal lesion detection with deep learning. *Journal of medical imaging* **5**, 036501-036501 (2018).
50. Quinton, F., *et al.* A tumour and liver automatic segmentation (atlas) dataset on contrast-enhanced magnetic resonance imaging for hepatocellular carcinoma. *Data* **8**, 79 (2023).
51. Aerts, H.J.W.L., Wee, L., Rios Velazquez, E., Leijenaar, R. T. H., Parmar, C., Grossmann, P., Carvalho, S., Bussink, J., Monshouwer, R., Haibe-Kains, B., Rietveld, D., Hoebers, F., Rietbergen, M. M., Leemans, C. R., Dekker, A., Quackenbush, J., Gillies, R. J., & Lambin, P. Data From NSCLC-Radiomics (Version 4) [Data set]. *The Cancer Imaging Archive*. (2019).

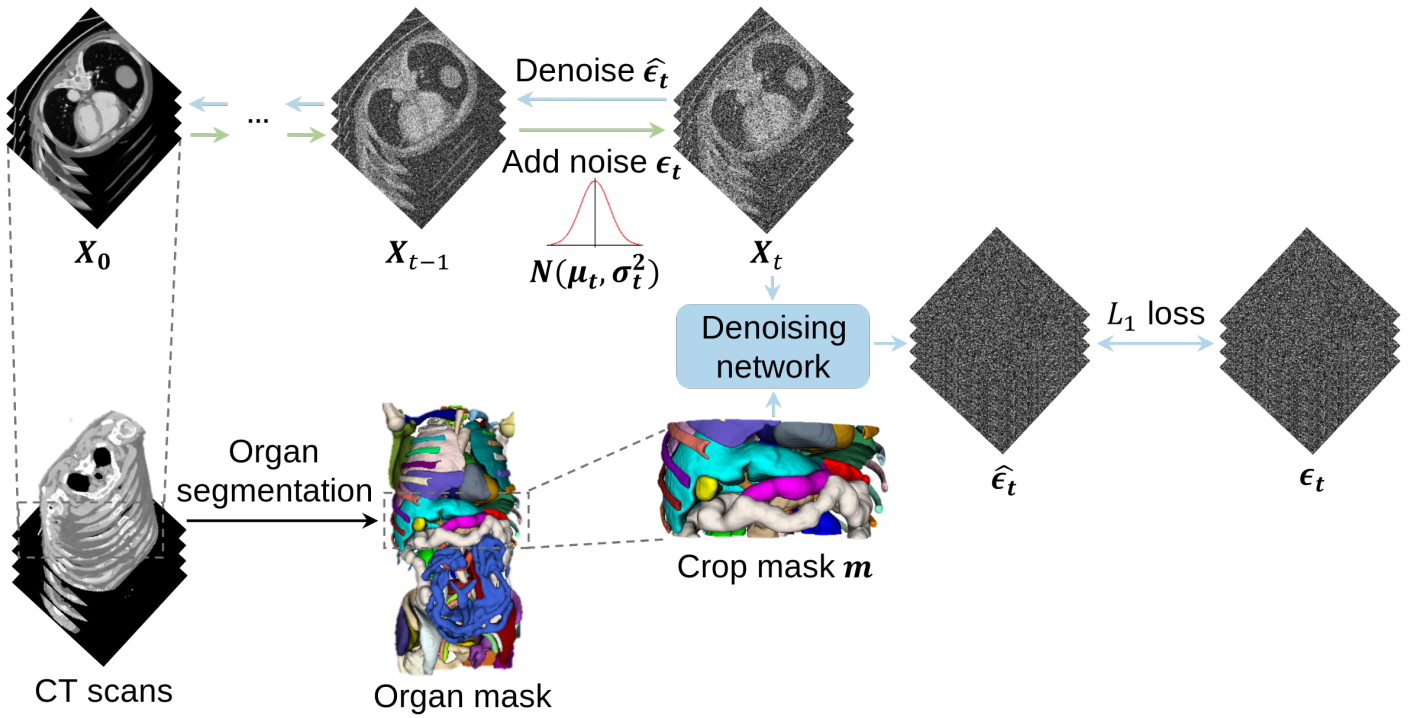
Acknowledgements This work was supported by the National Natural Science Foundation of China (62301311) (X.Z.), Shanghai Municipal Commission of Economy and Informatization (204694) (S.Z.), the Noncommunicable Chronic Diseases – National Science and Technology Major Project (2023ZD0501500) (Z.W.), the National Natural Science Foundation of China (U123A20457) (Z.W.), and the Traditional Chinese Medicine Multidisciplinary Innovation Team Program of Liaoning Province (LNZYYCXTD-JCCX-002) (Z.W.), National Natural Science Foundation of China (82203199) (H.C.).

Author contributions Conceptualization: W.L., H.C., X.Z., P.R., S.Z., and Z.W. Methodology: W.L., H.C., Z.Z., and L.L. Investigation: W.L., H.C., Z.Z., L.L., Q.X., Y.G., P.G., Y.J., C.W., G.W., T.X., and Y.Z. Visualization: W.L. and H.C. Funding acquisition: H.C., X.Z., S.Z., and Z.W. Supervision: X.Z., S.Z., and Z.W. Writing: W.L., H.C., and L.L.

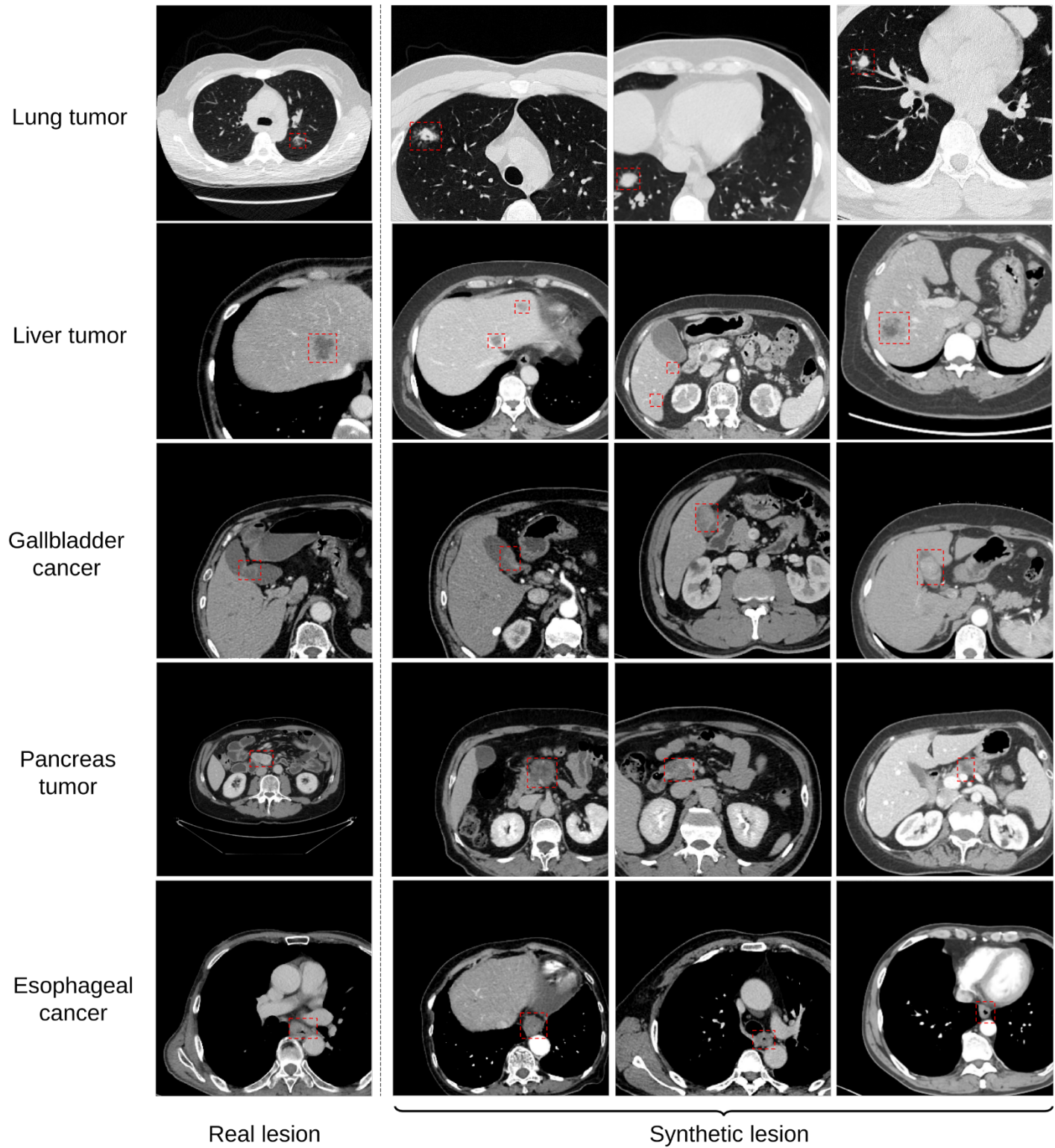
Competing interest The authors declare no competing interests.

Additional information

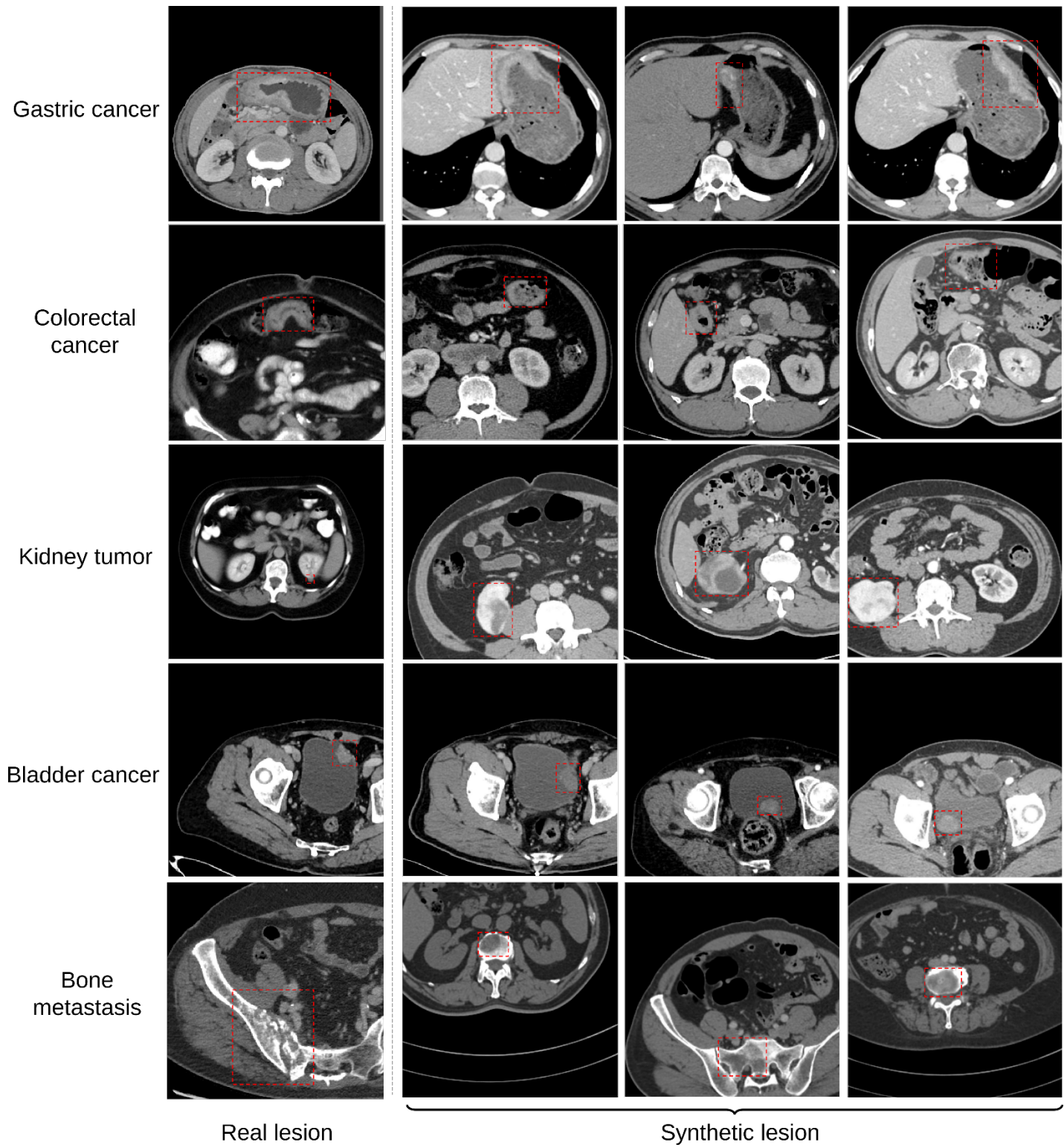
Correspondence and requests for materials should be addressed to Xiaofan Zhang, Shaoting Zhang or Zhenning Wang.



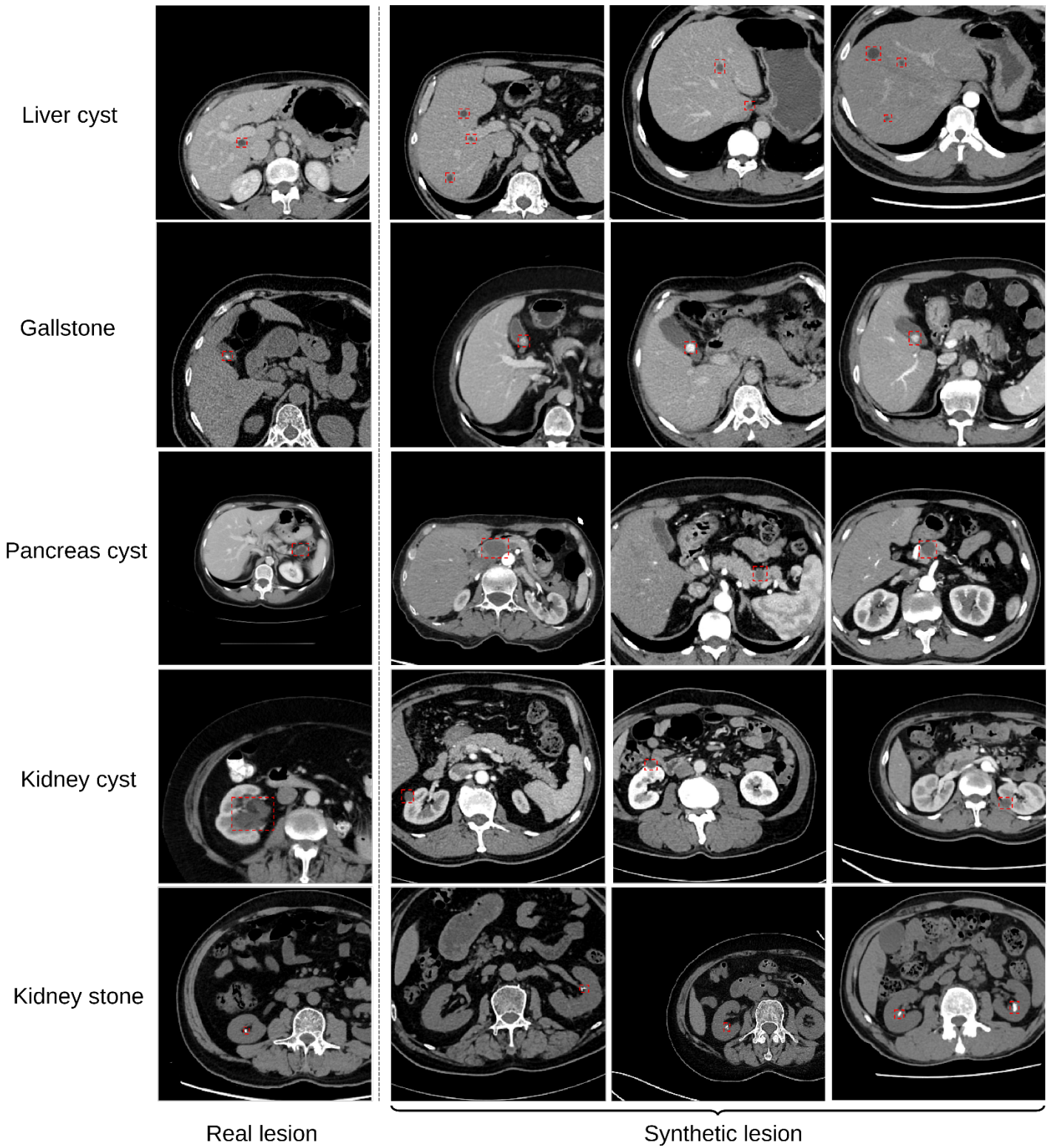
Extended Data Figure 1 | Overview of denoising network training process. During training, random Gaussian noise is added to the cropped original CT images (X_0), and the network learns to predict and remove this noise. The corresponding organ segmentation mask is concatenated as an input condition to guide the denoising process.



Extended Data Fig.2 | Examples from PASTA-Gen-30K (Part 1)



Extended Data Fig.2 | Examples from PASTA-Gen-30K (Part 2)



Extended Data Fig.2 | Examples from PASTA-Gen-30K (Part 3)

Extended Data Table 1 | Structured Attributes for Lesion Simulation in PASTA-Gen

Attribute	Definition	Structured descriptions/options
Enhancement status	Intravenous contrast agent usage	"Enhanced CT", "Non-contrast CT"
Location	Organ-specific anatomical regions	"Lung", "Liver", "Gallbladder", "Pancreas", "Esophagus", "Stomach", "Colorectal", "Kidney", "Bladder", "Bone"
Size	Dimensions across axial, sagittal, and coronal planes	Z×X×Y mm
Shape	Morphological characteristics of the lesion	"Round-like", "Irregular", "Wall thickening", "Punctate, nodular"
Density	Radiographic attenuation properties of the lesion	"Hypodense", "Isodense", "Hyperdense"
Heterogeneity	Uniformity of attenuation within the lesion	"Homogeneous", "Heterogeneous"
Surface	Features of the lesion's border and surface texture	"Well-defined margin", "Ill-defined margin"
Invasion	Invasion of or proximity to adjacent structures	"No close relationship with surrounding structures", "Close relationship with adjacent structures"

Extended Data Table 2 | Distribution of scan ranges in the in-house dataset.

Scan Range	No. of scans (%)
Thorax CT	5,642 (47.5%)
Abdomen-pelvis CT	1,601 (16.4%)
Thorax-abdomen-pelvis CT	763 (7.8%)
Others	2,761 (28.3%)
Total	10,767 (100.0%)

Extended Data Table 3 | Number of healthy organ scans in the template CT dataset

Organ	No. of scans
Healthy Lung	1,720
Contrast CT	0
Non-contrast CT	1,720
Healthy Liver	816
Contrast CT	600
Non-contrast CT	216
Healthy Gallbladder	1,901
Contrast CT	1,389
Non-contrast CT	512
Healthy Pancrease	2,222
Contrast CT	1,620
Non-contrast CT	602
Healthy Esophagus	752
Contrast CT	545
Non-contrast CT	207
Healthy Stomach	2,281
Contrast CT	1,664
Non-contrast CT	617
Healthy Colorectum	1,668
Contrast CT	1,292
Non-contrast CT	376
Healthy Kidney	975
Contrast CT	716
Non-contrast CT	259
Healthy Bladder	2,216
Contrast CT	1,616
Non-contrast CT	600
Healthy Trunk and Extremity	6,811
Bones	
Contrast CT	4,972
Non-contrast CT	1,839

Extended Data Table 4 | PASTA-Gen and PASTA Validation Datasets

Dataset name	Lesion target	No. of scans
Public datasets		
KiTS23	Kidney tumor, kidney cyst	489
MSD-Colon Tumor	Colon tumor	126
MSD-Liver Tumor	Liver tumor	303
MSD-Lung Tumor	Lung tumor	96
MSD-Pancreas*	Pancreatic tumor	216
MSD-Pancreas*	Pancreatic cyst	65
CMU datasets		
	Liver cyst	30
	Gallbladder cancer	30
	Gallstones	30
	Esophageal cancer	30
	Gastric cancer	30
	Kidney stone	30
	Bladder cancer	30
	Bone metastasis	30
Total		1,535

* MSD-Pancreas is reannotated to pancreatic tumor and pancreatic cyst.

Extended Data Table 5 | Composition of the Image Realism Evaluation Dataset

Lesion targets	No. of real CT scans	No. of synthetic CT scans
Lung tumor	50	50
Liver tumor	50	50
Gallbladder cancer	30	30
Pancreatic tumor	50	50
Esophageal Cancer	30	30
Gastric cancer	30	30
Colorectal cancer	50	50
Kidney tumor	50	50
Bladder cancer	30	30
Bone metastasis	30	30
Liver cyst	30	30
Gallstone	30	30
Pancreatic cyst	50	50
Kidney cyst	50	50
Kidney stone	30	30

Supplementary Table 1 | Comparison of Tumor Detection on Non-contrast CT Data Based on AUC.

	PASTA	PASTA (w/o pretraining)	Models Genesis	SuPerM	<i>p</i> -value*
Liver cancer	0.965 (0.950-0.985)	0.759 (0.737-0.804)	0.765 (0.725-0.823)	<u>0.855</u> <u>(0.817-0.911)</u>	0.031
Pancreatic cancer	0.987 (0.981-0.995)	0.597 (0.588-0.668)	0.774 (0.725-0.860)	<u>0.944</u> <u>(0.822-0.983)</u>	0.031
Kidney cancer	0.964 (0.954-0.983)	0.781 (0.743-0.836)	0.705 (0.767-0.800)	<u>0.908</u> <u>(0.870-0.942)</u>	0.031

The values in parentheses represent the minimum and maximum AUC values obtained across the 5-fold cross-validation.

* *p*-values were calculated using a one-sided Wilcoxon test comparing the **top-performing model** and the second-best model for each task

Supplementary Table 2 | Performance of Radiologists in Non-contrast CT Tumor Screening with and without PASTA-AID Assistance

	Liver Cancer				Pancreatic cancer				Kidney Cancer			
	TP	TN	FP	FN	TP	TN	FP	FN	TP	TN	FP	FN
Junior Radiologist 1												
Solo	5	37	3	3	2	24	1	4	5	45	2	4
PASTA-AID	9	63	0	1	10	31	1	0	11	61	1	0
Junior Radiologist 2												
Solo	7	38	2	3	5	27	0	5	6	44	1	4
PASTA-AID	10	59	1	1	9	30	0	2	10	68	0	2
Senior Radiologist 1												
Solo	11	50	4	2	9	42	2	2	14	65	2	3
PASTA-AID	15	56	1	1	8	44	1	1	14	72	1	1
Senior Radiologist 2												
Solo	10	53	4	3	8	53	3	2	12	59	3	4
PASTA-AID	14	61	0	2	10	61	2	0	13	68	0	2
Avg. Cases Read (Solo)	58.8				47.3				68.3			
Avg. Cases Read (PASTA-AID)	73.5				52.5				81.0			
Efficiency Improvement (%)	25.1				11.1				18.7			
Avg. Recall (Solo, %)	73.5				61.3				68.2			
Avg. Recall (PASTA-AID, %)	90.5				92.7				90.8			
Recall Improvement (%)	17.0				31.4				22.6			
<i>p</i> -value for recall	0.043				0.002				0.010			
Avg. Precision (Solo, %)	71.3				80.3				81.2			
Avg. Precision (PASTA-AID, %)	96.2				90.8				96.3			
Precision Improvement (%)	24.9				10.5				15.1			
<i>p</i> -value for precision	0.001				0.279				0.027			

TP, true positive; TN, true negative; FP, false positive; FN, false negative.

Reading time for each round was limited to 30 minutes.

p-values were calculated using a two-sided Cochran–Mantel–Haenszel test stratified by reader across four radiologists, comparing PASTA-AID assisted versus solo readings for each diagnostic metric.

Supplementary Table 3 | Sufficient Data and Few-Shot Segmentation DSC across Models.

	PASTA	Models Genesis	SuPerM	nnUNet	Universal	p-value*
Lung tumor						
No. of Few-shot						
Samples†						
1	0.529 (0.458-0.599)	0.179 (0.127-0.230)	<u>0.302</u> <u>(0.230-0.383)</u>	0.188 (0.133-0.254)	0.167 (0.118-0.219)	<0.001
2	0.622 (0.559-0.683)	0.358 (0.291-0.425)	<u>0.383</u> <u>(0.310-0.457)</u>	0.288 (0.220-0.360)	0.266 (0.203-0.330)	<0.001
4	0.680 (0.621-0.728)	0.396 (0.321-0.464)	<u>0.513</u> <u>(0.444-0.590)</u>	0.335 (0.265-0.405)	0.307 (0.247-0.378)	<0.001
8	0.709 (0.656-0.757)	0.365 (0.309-0.423)	<u>0.605</u> <u>(0.546-0.660)</u>	0.323 (0.257-0.389)	0.293 (0.233-0.361)	<0.001
16	0.706 (0.651-0.751)	0.261 (0.206-0.322)	<u>0.591</u> <u>(0.531-0.654)</u>	0.106 (0.073-0.142)	0.088 (0.059-0.121)	<0.001
Full-scale data	0.708	0.680	0.661	<u>0.689</u>	0.661	
training (n=64)	(0.639-0.767)	(0.616-0.735)	(0.595-0.720)	<u>(0.630-0.744)</u>	(0.602-0.708)	0.018
Liver tumor						
No. of Few-shot						
Samples†						
1	0.243 (0.199-0.290)	0.101 (0.078-0.129)	<u>0.194</u> <u>(0.148-0.247)</u>	0.097 (0.070-0.125)	0.080 (0.057-0.106)	0.004
2	0.477 (0.430-0.527)	0.145 (0.112-0.176)	<u>0.313</u> <u>(0.258-0.369)</u>	0.164 (0.133-0.202)	0.141 (0.110-0.176)	<0.001
4	0.598 (0.548-0.643)	0.193 (0.157-0.233)	<u>0.392</u> <u>(0.341-0.451)</u>	0.170 (0.134-0.206)	0.152 (0.121-0.186)	<0.001
8	0.617 (0.568-0.658)	0.108 (0.081-0.138)	<u>0.390</u> <u>(0.334-0.447)</u>	0.064 (0.041-0.090)	0.060 (0.040-0.084)	<0.001
16	0.629 (0.580-0.677)	0.131 (0.100-0.164)	<u>0.316</u> <u>(0.261-0.376)</u>	0.018 (0.011-0.025)	0.012 (0.008-0.016)	<0.001
Full-scale data	0.696	<u>0.673</u>	0.654	0.666	0.640	
training (n=131)	(0.652-0.738)	<u>(0.627-0.716)</u>	(0.607-0.701)	(0.619-0.713)	(0.591-0.687)	<0.001
Gallbladder cancer						
No. of Few-shot						
Samples†						
1	0.565 (0.454-0.673)	<u>0.112</u> <u>(0.062-0.171)</u>	0.065 (0.009-0.131)	0.101 (0.051-0.160)	0.096 (0.042-0.152)	<0.001
2	0.608 (0.509-0.696)	0.122 (0.067-0.179)	<u>0.145</u> <u>(0.074-0.226)</u>	0.104 (0.055-0.162)	0.095 (0.046-0.153)	<0.001
4	0.649 (0.554-0.736)	0.079 (0.039-0.125)	<u>0.217</u> <u>(0.137-0.301)</u>	0.152 (0.097-0.216)	0.130 (0.080-0.190)	<0.001
8	0.630	0.206	<u>0.419</u>	0.203	0.181	<0.001

	(0.528-0.721)	(0.128-0.286)	<u>(0.317-0.518)</u>	(0.137-0.269)	(0.116-0.242)	
16	0.653	0.107	<u>0.365</u>	0.105	0.081	<0.001
	(0.544-0.748)	(0.059-0.158)	<u>(0.268-0.465)</u>	(0.065-0.148)	(0.047-0.116)	
Full-scale data training (n=30)	0.654	0.598	0.575	<u>0.644</u>	0.613	0.464
	(0.556-0.744)	(0.484-0.700)	(0.470-0.671)	<u>(0.541-0.742)</u>	(0.517-0.708)	

Pancreatic tumor

No. of Few-shot						
Samples†						
1	0.158	0.037	0.041	<u>0.046</u>	0.040	<0.001
	(0.133-0.186)	(0.024-0.052)	(0.027-0.058)	<u>(0.032-0.062)</u>	(0.026-0.054)	
2	0.216	0.073	<u>0.079</u>	0.055	0.051	<0.001
	(0.187-0.252)	(0.054-0.092)	<u>(0.060-0.101)</u>	(0.038-0.075)	(0.035-0.065)	
4	0.209	0.015	<u>0.122</u>	0.005	0.007	<0.001
	(0.175-0.244)	(0.007-0.026)	<u>(0.096-0.150)</u>	(0.002-0.010)	(0.004-0.010)	
8	0.335	0.043	<u>0.141</u>	0.000	0.005	<0.001
	(0.294-0.375)	(0.029-0.057)	<u>(0.113-0.169)</u>	(0.000-0.000)	(0.004-0.006)	
16	0.414	0.066	<u>0.207</u>	0.000	0.005	<0.001
	(0.374-0.454)	(0.049-0.085)	<u>(0.176-0.241)</u>	(0.000-0.000)	(0.004-0.007)	
Full-scale data training (n=220)	0.510	0.482	0.408	<u>0.491</u>	0.468	0.010
	(0.468-0.551)	(0.442-0.520)	(0.365-0.449)	<u>(0.452-0.531)</u>	(0.428-0.508)	

Esophageal Cancer

No. of Few-shot						
Samples†						
1	0.577	0.166	<u>0.319</u>	0.175	0.163	<0.001
	(0.466-0.683)	(0.089-0.253)	<u>(0.218-0.419)</u>	(0.089-0.268)	(0.089-0.248)	
2	0.608	0.279	<u>0.422</u>	0.351	0.323	<0.001
	(0.507-0.698)	(0.184-0.377)	<u>(0.324-0.518)</u>	(0.254-0.458)	(0.232-0.417)	
4	0.620	<u>0.458</u>	0.384	0.350	0.312	<0.001
	(0.520-0.719)	<u>(0.357-0.552)</u>	(0.255-0.512)	(0.242-0.464)	(0.214-0.415)	
8	0.659	0.345	0.491	<u>0.506</u>	0.476	<0.001
	(0.555-0.758)	(0.234-0.460)	(0.376-0.604)	<u>(0.405-0.605)</u>	(0.389-0.566)	
16	0.684	0.385	<u>0.624</u>	0.562	0.526	0.007
	(0.582-0.775)	(0.275-0.500)	<u>(0.527-0.709)</u>	(0.481-0.637)	(0.447-0.604)	
Full-scale data training (n=30)	0.683	0.635	<u>0.646</u>	0.634	0.602	0.004
	(0.576-0.783)	(0.508-0.741)	<u>(0.535-0.746)</u>	(0.514-0.739)	(0.479-0.703)	

Gastric Cancer

No. of Few-shot						
Samples†						
1	0.309	<u>0.074</u>	0.045	0.054	0.045	<0.001
	(0.209-0.418)	<u>(0.039-0.110)</u>	(0.015-0.083)	(0.021-0.091)	(0.017-0.080)	
2	0.494	<u>0.098</u>	0.033	0.090	0.067	<0.001
	(0.413-0.574)	<u>(0.056-0.142)</u>	(0.013-0.056)	(0.049-0.132)	(0.031-0.112)	
4	0.548	0.183	<u>0.235</u>	0.165	0.135	<0.001
	(0.469-0.623)	(0.129-0.241)	<u>(0.165-0.302)</u>	(0.110-0.220)	(0.081-0.190)	
8	0.584	0.222	<u>0.383</u>	0.217	0.185	<0.001

	(0.505-0.655)	(0.159-0.293)	<u>(0.295-0.455)</u>	(0.161-0.276)	(0.129-0.245)	
16	0.615	0.275	<u>0.461</u>	0.247	0.203	<0.001
	(0.544-0.677)	(0.219-0.330)	<u>(0.398-0.524)</u>	(0.204-0.288)	(0.162-0.241)	
Full-scale data training (n=30)	0.627	0.561	0.544	<u>0.581</u>	0.554	0.004
(0.542-0.697)	(0.496-0.631)	(0.460-0.617)	<u>(0.505-0.646)</u>	(0.486-0.624)		

Colon Cancer

No. of Few-shot Samples†						
1	0.044	0.006	<u>0.019</u>	0.005	0.008	0.001
	(0.027-0.066)	(0.000-0.015)	<u>(0.008-0.034)</u>	(0.002-0.008)	(0.006-0.010)	
2	0.167	0.024	<u>0.050</u>	0.023	0.026	<0.001
	(0.126-0.208)	(0.012-0.041)	<u>(0.029-0.071)</u>	(0.011-0.038)	(0.014-0.040)	
4	0.245	0.042	<u>0.115</u>	0.061	0.050	<0.001
	(0.204-0.292)	(0.024-0.064)	<u>(0.083-0.147)</u>	(0.042-0.085)	(0.031-0.069)	
8	0.290	0.082	<u>0.148</u>	0.093	0.077	<0.001
	(0.240-0.343)	(0.059-0.107)	<u>(0.117-0.182)</u>	(0.069-0.119)	(0.054-0.101)	
16	0.391	<u>0.112</u>	0.110	0.059	0.043	<0.001
	(0.338-0.445)	<u>(0.086-0.142)</u>	(0.083-0.139)	(0.046-0.074)	(0.031-0.056)	
Full-scale data training (n=126)	0.517	0.496	0.481	<u>0.517</u>	0.491	0.901
	(0.458-0.583)	(0.436-0.556)	(0.425-0.542)	<u>(0.454-0.576)</u>	(0.438-0.547)	

Kidney tumor

No. of Few-shot Samples†						
1	0.246	0.039	<u>0.072</u>	0.052	0.043	<0.001
	(0.220-0.271)	(0.030-0.049)	<u>(0.059-0.086)</u>	(0.042-0.061)	(0.034-0.052)	
2	0.301	0.015	<u>0.127</u>	0.046	0.037	<0.001
	(0.269-0.330)	(0.010-0.019)	<u>(0.110-0.146)</u>	(0.037-0.054)	(0.030-0.046)	
4	0.394	0.006	<u>0.174</u>	0.021	0.021	<0.001
	(0.361-0.428)	(0.003-0.010)	<u>(0.152-0.198)</u>	(0.014-0.029)	(0.014-0.027)	
8	0.632	0.133	<u>0.254</u>	0.143	0.124	<0.001
	(0.606-0.658)	(0.116-0.150)	<u>(0.229-0.279)</u>	(0.128-0.159)	(0.107-0.139)	
16	0.678	0.144	<u>0.336</u>	0.051	0.046	<0.001
	(0.654-0.706)	(0.129-0.161)	<u>(0.309-0.361)</u>	(0.042-0.062)	(0.036-0.055)	
Full-scale data training (n=489)	0.814	<u>0.800</u>	0.722	0.784	0.756	<0.001
	(0.793-0.834)	<u>(0.780-0.819)</u>	(0.695-0.748)	(0.763-0.805)	(0.736-0.776)	

Bladder cancer

No. of Few-shot Samples†						
1	0.509	<u>0.136</u>	0.052	0.081	0.075	<0.001
	(0.381-0.631)	<u>(0.064-0.213)</u>	(0.000-0.122)	(0.018-0.158)	(0.014-0.152)	
2	0.667	<u>0.290</u>	0.194	0.219	0.201	<0.001
	(0.566-0.764)	<u>(0.196-0.396)</u>	(0.105-0.294)	(0.140-0.311)	(0.115-0.297)	
4	0.697	<u>0.445</u>	0.396	0.360	0.332	<0.001
	(0.600-0.781)	<u>(0.355-0.535)</u>	(0.289-0.500)	(0.264-0.461)	(0.242-0.426)	
8	0.712	<u>0.500</u>	0.441	0.318	0.289	<0.001

	(0.611-0.797)	<u>(0.400-0.588)</u>	(0.325-0.553)	(0.215-0.421)	(0.194-0.385)	
16	0.757	<u>0.550</u>	0.309	0.331	0.301	<0.001
	(0.674-0.828)	<u>(0.466-0.637)</u>	(0.226-0.394)	(0.230-0.432)	(0.205-0.404)	
Full-scale data training (n=30)	0.790	<u>0.769</u>	0.660	0.759	0.738	0.127
(0.717-0.844)	<u>(0.694-0.830)</u>	(0.550-0.756)	(0.680-0.829)	(0.658-0.806)		

Bone metastasis

No. of Few-shot						
Samples†						
1	0.313	0.064	0.063	<u>0.067</u>	0.065	<0.001
	(0.266-0.386)	(0.015-0.120)	(0.019-0.122)	<u>(0.021-0.124)</u>	(0.020-0.123)	
2	0.360	0.049	0.050	<u>0.058</u>	0.050	<0.001
	(0.251-0.421)	(0.001-0.118)	(0.009-0.106)	<u>(0.011-0.128)</u>	(0.007-0.111)	
4	0.371	0.068	0.053	<u>0.076</u>	0.064	<0.001
	(0.287-0.458)	(0.023-0.123)	(0.013-0.108)	<u>(0.026-0.135)</u>	(0.022-0.113)	
8	0.402	<u>0.124</u>	0.060	0.081	0.074	<0.001
	(0.298-0.485)	<u>(0.059-0.205)</u>	(0.020-0.115)	(0.033-0.138)	(0.025-0.145)	
16	0.432	<u>0.023</u>	0.002	0.031	0.023	<0.001
	(0.267-0.538)	<u>(0.010-0.040)</u>	(0.000-0.007)	(0.011-0.058)	(0.006-0.051)	
Full-scale data training (n=30)	0.433	0.321	<u>0.389</u>	0.376	0.346	0.020
	(0.317-0.574)	(0.210-0.431)	<u>(0.284-0.489)</u>	(0.252-0.488)	(0.245-0.458)	

Liver cyst

No. of Few-shot						
Samples†						
1	0.639	0.015	<u>0.286</u>	0.000	0.009	<0.001
	(0.545-0.727)	(0.000-0.042)	<u>(0.172-0.407)</u>	(0.000-0.000)	(0.004-0.015)	
2	0.631	0.038	<u>0.199</u>	0.000	0.006	<0.001
	(0.533-0.740)	(0.008-0.075)	<u>(0.087-0.328)</u>	(0.000-0.000)	(0.003-0.010)	
4	0.748	0.022	<u>0.315</u>	0.000	0.004	<0.001
	(0.671-0.814)	(0.001-0.050)	<u>(0.204-0.436)</u>	(0.000-0.000)	(0.001-0.008)	
8	0.716	0.056	<u>0.271</u>	0.000	0.002	<0.001
	(0.619-0.802)	(0.009-0.114)	<u>(0.161-0.391)</u>	(0.000-0.000)	(0.000-0.006)	
16	0.789	0.010	<u>0.299</u>	0.000	0.002	<0.001
	(0.694-0.854)	(0.001-0.025)	<u>(0.165-0.454)</u>	(0.000-0.000)	(0.000-0.005)	
Full-scale data training (n=30)	0.755	0.713	<u>0.724</u>	0.716	0.686	<0.001
	(0.649-0.846)	(0.611-0.799)	<u>(0.628-0.802)</u>	(0.612-0.794)	(0.588-0.773)	

Gallstone

No. of Few-shot						
Samples†						
1	0.444	<u>0.100</u>	0.072	0.092	0.087	<0.001
	(0.312-0.581)	<u>(0.030-0.182)</u>	(0.000-0.153)	(0.022-0.185)	(0.024-0.172)	
2	0.637	0.190	0.254	<u>0.280</u>	0.247	<0.001
	(0.531-0.732)	(0.097-0.286)	(0.159-0.354)	<u>(0.164-0.396)</u>	(0.145-0.354)	
4	0.687	0.321	<u>0.364</u>	0.348	0.329	<0.001
	(0.589-0.776)	(0.208-0.427)	<u>(0.254-0.486)</u>	(0.244-0.454)	(0.226-0.437)	
8	0.769	0.493	0.366	<u>0.510</u>	0.477	<0.001

	(0.692-0.829)	(0.368-0.611)	(0.255-0.492)	<u>(0.397-0.619)</u>	(0.360-0.580)	
16	0.762	<u>0.465</u>	0.133	0.356	0.337	<0.001
	(0.684-0.833)	<u>(0.352-0.580)</u>	(0.048-0.234)	(0.244-0.471)	(0.226-0.457)	
Full-scale data training (n=30)	<u>0.781</u>	0.760	0.754	0.785	0.756	0.358

Pancreatic cyst

No. of Few-shot

Samples†

1	0.465	0.077	<u>0.099</u>	0.056	0.055	<0.001
	(0.382-0.541)	(0.043-0.118)	<u>(0.054-0.153)</u>	(0.022-0.100)	(0.023-0.092)	
2	0.460	0.104	<u>0.130</u>	0.081	0.075	<0.001
	(0.375-0.546)	(0.054-0.156)	<u>(0.074-0.197)</u>	(0.040-0.132)	(0.040-0.118)	
4	0.515	0.203	<u>0.261</u>	0.179	0.162	<0.001
	(0.428-0.609)	(0.138-0.277)	<u>(0.178-0.352)</u>	(0.109-0.252)	(0.099-0.229)	
8	0.641	0.220	<u>0.458</u>	0.187	0.175	<0.001
	(0.552-0.710)	(0.158-0.285)	<u>(0.389-0.534)</u>	(0.119-0.253)	(0.115-0.241)	
16	0.707	0.308	<u>0.497</u>	0.092	0.082	<0.001
	(0.636-0.768)	(0.239-0.378)	<u>(0.412-0.579)</u>	(0.048-0.140)	(0.044-0.125)	
Full-scale data training (n=61)	0.722	0.680	0.637	<u>0.715</u>	0.682	0.020
	(0.653-0.788)	(0.599-0.751)	(0.555-0.712)	<u>(0.641-0.779)</u>	(0.606-0.750)	

Kidney cyst

No. of Few-shot

Samples†

1	0.161	0.045	0.048	<u>0.056</u>	0.054	<0.001
	(0.132-0.192)	(0.030-0.061)	(0.033-0.066)	<u>(0.039-0.076)</u>	(0.038-0.071)	
2	0.137	<u>0.013</u>	0.010	0.000	0.005	<0.001
	(0.108-0.167)	<u>(0.006-0.021)</u>	(0.004-0.019)	(0.000-0.000)	(0.004-0.007)	
4	0.141	0.004	0.000	0.000	<u>0.005</u>	<0.001
	(0.114-0.171)	(0.001-0.009)	(0.000-0.000)	(0.000-0.000)	<u>(0.004-0.006)</u>	
8	0.102	0.000	0.000	0.000	<u>0.005</u>	<0.001
	(0.077-0.127)	(0.000-0.000)	(0.000-0.000)	(0.000-0.000)	<u>(0.004-0.007)</u>	
16	0.289	0.000	0.000	0.000	<u>0.005</u>	<0.001
	(0.252-0.329)	(0.000-0.000)	(0.000-0.000)	(0.000-0.000)	<u>(0.004-0.006)</u>	
Full-scale data training (n=489)	0.660	<u>0.641</u>	0.616	0.624	0.598	<0.001
	(0.622-0.696)	<u>(0.607-0.677)</u>	(0.582-0.649)	(0.589-0.655)	(0.562-0.630)	

Kidney stone

No. of Few-shot

Samples†

1	0.464	0.000	0.000	0.000	<u>0.002</u>	<0.001
	(0.350-0.573)	(0.000-0.000)	(0.000-0.000)	(0.000-0.000)	<u>(0.000-0.005)</u>	
2	0.678	0.000	0.000	0.000	<u>0.005</u>	<0.001
	(0.622-0.730)	(0.000-0.000)	(0.000-0.000)	(0.000-0.000)	<u>(0.002-0.009)</u>	
4	0.780	0.000	0.000	0.000	<u>0.006</u>	<0.001
	(0.733-0.819)	(0.000-0.000)	(0.000-0.000)	(0.000-0.000)	<u>(0.002-0.011)</u>	
8	0.636	0.000	0.000	0.000	<u>0.005</u>	<0.001

	(0.502-0.752)	(0.000-0.000)	(0.000-0.000)	(0.000-0.000)	<u>(0.001-0.009)</u>	
16	0.822	0.004	0.000	0.000	<u>0.005</u>	<0.001
	(0.799-0.844)	(0.000-0.011)	(0.000-0.000)	(0.000-0.000)	<u>(0.001-0.009)</u>	
Full-scale data training (n=30)	0.777	0.755	<u>0.768</u>	0.755	0.724	0.261
(0.713-0.820)	(0.682-0.809)	<u>(0.707-0.814)</u>	(0.675-0.823)	(0.638-0.789)		

Brain tumor (MRI)

No. of Few-shot

Samples†

1	0.310 (0.288-0.333)	0.303	<u>0.312</u> <u>(0.287-0.337)</u>	0.288	0.253	0.208
2	0.344 (0.318-0.372)	0.290	<u>0.310</u> <u>(0.287-0.333)</u>	0.270	0.240	<0.001
4	0.438 (0.415-0.462)	0.376	<u>0.403</u> <u>(0.376-0.428)</u>	0.348	0.315	<0.001
8	0.465 (0.441-0.488)	0.420	<u>0.450</u> <u>(0.425-0.475)</u>	0.423	0.386	0.011
16	0.504 (0.479-0.528)	0.447	<u>0.468</u> <u>(0.443-0.490)</u>	0.457	0.418	<0.001

Liver tumor (MRI)

No. of Few-shot

Samples†

1	0.267 (0.219-0.315)	0.211	<u>0.237</u> <u>(0.185-0.287)</u>	0.213	0.181	0.030
2	0.339 (0.282-0.397)	0.225	<u>0.232</u> <u>(0.185-0.291)</u>	0.193	0.166	<0.001
4	0.492 (0.422-0.555)	0.284	<u>0.341</u> <u>(0.279-0.405)</u>	0.252	0.232	<0.001
8	0.562 (0.495-0.628)	0.289	<u>0.430</u> <u>(0.368-0.501)</u>	0.296	0.264	<0.001
16	0.603 (0.532-0.672)	0.292	<u>0.469</u> <u>(0.400-0.540)</u>	0.283	0.244	<0.001

Non-parametric bootstrapping with 1,000 bootstrap replicates is employed for statistical analysis. The 95% CI is included in parentheses.

* *p*-values were calculated using a one-sided Wilcoxon test comparing the **top-performing model** and the second-best model for each task

† 2000 iterations.

Supplementary Table 4 | Annotation and Reporting Efficiency of Radiologists across Lesion Types and Experience Levels with and without PASTA-AID Assistance

	Liver Cancer		Pancreatic cancer		Kidney Cancer	
	T_mask	T_report	T_mask	T_report	T_mask	T_report
Junior Radiologist 1						
Solo (n=50)	590.3 (534.0, 646.6)	197.4 (179.4, 215.5)	341.8 (303.2, 380.3)	175.7 (159.8, 191.7)	286.1 (265.9, 306.3)	137.4 (118.9, 156.0)
PASTA-AID (n=50)	294.8 (239.9, 349.6)	146.5 (133.2, 159.9)	80.8 (74.8, 86.8)	122.4 (111.4, 133.3)	62.0 (51.0, 73.0)	121.1 (103.6, 138.6)
Junior Radiologist 2						
Solo (n=50)	597.0 (551.3, 642.6)	189.0 (171.3, 206.6)	321.2 (287.3, 355.1)	173.5 (160.3, 186.8)	298.9 (278.2, 319.7)	143.8 (127.5, 160.2)
PASTA-AID (n=50)	299.1 (252.5, 345.8)	147.1 (133.8, 160.3)	81.9 (75.9, 87.9)	108.0 (97.1, 118.9)	65.5 (55.6, 75.5)	116.1 (104.8, 127.4)
<i>p</i> -value	<0.001	<0.001	<0.001	<0.001	<0.001	0.006
Overall time reduction (%)	50.0	24.0	75.5	34.0	78.2	15.7
Senior Radiologist 1						
Solo (n=50)	495.4 (451.0, 539.7)	157.6 (138.7, 176.6)	263.6 (232.7, 294.5)	144.9 (135.9, 153.9)	235.1 (220.3, 249.9)	136.2 (125.1, 147.3)
PASTA-AID (n=50)	251.2 (196.9, 305.6)	126.6 (112.9, 140.2)	67.9 (62.4, 73.5)	103.7 (96.7, 110.7)	59.0 (46.0, 72.1)	92.5 (83.4, 101.6)
Senior Radiologist 2						
Solo (n=50)	477.4 (437.8, 517.0)	152.8 (135.9, 169.8)	238.6 (216.6, 260.7)	135.6 (127.6, 143.6)	226.8 (212.4, 241.1)	142.5 (131.9, 153.1)
PASTA-AID (n=50)	280.4 (239.9, 321.0)	116.1 (101.6, 130.6)	70.6 (65.1, 76.0)	111.5 (102.7, 120.4)	58.7 (46.2, 71.2)	84.5 (75.7, 93.3)
<i>p</i> -value*	<0.001	<0.001	<0.001	<0.001	<0.001	<0.001
Overall time reduction (%)	45.3	21.8	72.4	23.3	74.5	36.5

T_mask: mask annotation time (seconds), T_report: report generation time (seconds).

Time-related data within each cell are presented as mean (95% CI).

* *p*-values were calculated using a linear mixed-effects model with doctor as a random intercept.

Supplementary Table 5 | Performance Improvement of Junior Radiologists with PASTA-AID Assistance

	Liver Cancer		Pancreatic cancer		Kidney Cancer	
	Dice	Accuracy	Dice	Accuracy	Dice	Accuracy
Junior Radiologist 1						
Solo (n=50)	0.740 (0.677, 0.803)	0.940 (0.914, 0.966)	0.740 (0.649, 0.832)	0.908 (0.875, 0.941)	0.752 (0.704, 0.799)	0.932 (0.902, 0.962)
PASTA-AID (n=50)	0.805 (0.744, 0.866)	0.948 (0.920, 0.976)	0.850 (0.784, 0.917)	0.920 (0.890, 0.950)	0.818 (0.763, 0.872)	0.944 (0.918, 0.970)
Junior Radiologist 2						
Solo (n=50)	0.702 (0.628, 0.776)	0.928 (0.898, 0.958)	0.764 (0.703, 0.826)	0.924 (0.894, 0.954)	0.715 (0.659, 0.772)	0.920 (0.888, 0.952)
PASTA-AID (n=50)	0.813 (0.740, 0.887)	0.924 (0.892, 0.956)	0.832 (0.777, 0.886)	0.936 (0.909, 0.963)	0.826 (0.771, 0.880)	0.916 (0.883, 0.949)
Performance Improvement (%)	12.2	0.2	11.8	1.3	12.0	0.4
p-value	0.011	0.890	0.017	0.422	0.001	0.790

Dice: image overlap ratio, acc: accuracy of structured reports.

Dice scores for image overlap and accuracy rates of structured reports within each cell are presented as mean (95% CI).

* p-values were calculated using a linear mixed-effects model with doctor as a random intercept.

Supplementary Table 6 | Accuracy and F1-Scores of Various Models in Structured Report Generation

	PASTA	UNet	Models Genesis	SuPerM	<i>p</i> -value*
Shape					
ACC	0.849 <u>(0.831-0.866)</u>	<u>0.789</u> <u>(0.769-0.809)</u>	0.660 (0.636-0.681)	0.788 (0.767-0.807)	<0.001
F1-score	0.781 <u>(0.738-0.818)</u>	0.688 (0.645-0.730)	0.199 (0.194-0.203)	<u>0.742</u> <u>(0.701-0.775)</u>	0.017
Invasion					
ACC	0.815 <u>(0.797-0.833)</u>	0.793 (0.772-0.815)	0.754 (0.732-0.775)	<u>0.810</u> <u>(0.790-0.830)</u>	0.319
F1-score	<u>0.723</u> <u>(0.699-0.749)</u>	0.700 (0.672-0.728)	0.430 (0.422-0.437)	0.732 (0.706-0.759)	0.730
Density					
ACC	0.726 <u>(0.702-0.746)</u>	<u>0.689</u> <u>(0.667-0.711)</u>	0.529 (0.503-0.553)	0.637 (0.612-0.662)	<0.001
F1-score	0.684 <u>(0.657-0.706)</u>	<u>0.644</u> <u>(0.617-0.668)</u>	0.334 (0.315-0.352)	0.589 (0.561-0.615)	<0.001
Heterogeneity					
ACC	0.903 <u>(0.889-0.917)</u>	<u>0.871</u> <u>(0.854-0.888)</u>	0.752 (0.729-0.771)	0.829 (0.810-0.848)	<0.001
F1-score	0.868 <u>(0.849-0.887)</u>	<u>0.825</u> <u>(0.802-0.847)</u>	0.429 (0.422-0.435)	0.762 (0.735-0.787)	<0.001
Surface					
ACC	0.891 <u>(0.875-0.907)</u>	<u>0.863</u> <u>(0.845-0.880)</u>	0.722 (0.702-0.744)	0.811 (0.791-0.830)	<0.001
F1-score	0.863 <u>(0.843-0.883)</u>	<u>0.825</u> <u>(0.802-0.847)</u>	0.419 (0.413-0.427)	0.754 (0.729-0.779)	<0.001

Non-parametric bootstrapping with 1,000 bootstrap replicates is employed for statistical analysis. The 95% CI is included in parentheses.

* *p*-values were calculated using a one-sided permutation test with 10,000 permutations comparing the **top-performing model** and the second-best model for each task

Supplementary Table 7 | Comparison of Tumor Staging and Survival Prediction AUC Values.

	PASTA	Models Genesis	SuPerM	FMCIB	<i>p</i> -value*
Tumor staging					
Gastric cancer	0.770 (0.636-0.858)	0.548 (0.456-0.656)	0.618 (0.520-0.751)	0.741 (0.593-0.851)	0.031
Rectal cancer	0.738 (0.643-0.846)	0.646 (0.617-0.683)	0.613 (0.421-0.804)	0.645 (0.461-0.779)	0.031
Bladder cancer	0.855 (0.750-0.950)	0.633 (0.489-0.800)	0.648 (0.500-0.889)	0.689 (0.646-0.756)	0.031
Survival prediction					
Lung cancer	0.700 (0.595-0.779)	0.650 (0.562-0.701)	0.687 (0.597-0.730)	0.617 (0.591-0.660)	0.156
Gastric cancer	0.660 (0.525-0.784)	0.546 (0.480-0.652)	0.508 (0.344-0.647)	0.626 (0.481-0.763)	0.031
Rectal cancer	0.759 (0.718-0.858)	0.626 (0.468-0.750)	0.714 (0.656-0.790)	0.713 (0.613-0.805)	0.094
Bladder cancer	0.878 (0.750-1.000)	0.844 (0.722-1.000)	0.838 (0.700-1.000)	0.843 (0.750-1.000)	0.500

The values in parentheses represent the minimum and maximum AUC values obtained across the 5-fold cross-validation.

* *p*-values were calculated using a one-sided Wilcoxon test comparing the **top-performing model** and the **second-best model** for each task

Supplementary Table 8 | CT modalities selected as templates for simulating each lesion in PASTA-Gen

Lesion	Modality of template CT
Lung tumor	Non-contrast CT
Liver tumor	Enhanced CT
Gallbladder cancer	Enhanced CT
Pancreatic tumor	Enhanced CT
Esophageal Cancer	Enhanced CT
Gastric cancer	Enhanced CT
Colorectal cancer	Enhanced CT
Kidney tumor	Enhanced CT
Bladder cancer	Enhanced CT
Bone metastasis	Enhanced CT
Liver cyst	Enhanced CT & Non-contrast CT
Gallstone	Enhanced CT & Non-contrast CT
Pancreatic cyst	Enhanced CT
Kidney cyst	Enhanced CT
Kidney stone	Non-contrast CT

Supplementary Table 9 | Class name and value in PASTA-Gen-30K

Lesion	Value
Lung	1
Liver	2
Gallbladder	3
Pancreas	4
Esophagus	5
Stomach	6
Colon & rectal	7
Kidney	8
Bladder	9
Bone	10
Lung tumor	11
Liver tumor	12
Gallbladder cancer	13
Pancreatic tumor	14
Esophageal Cancer	15
Gastric cancer	16
Colorectal cancer	17
Kidney tumor	18
Bladder cancer	19
Bone metastasis	20
Liver cyst	21
Gallstone	22
Pancreatic cyst	23
Kidney cyst	24
Kidney stone	25